Extreme precipitation associated with atmospheric rivers over West Antarctic ice shelves: insights from kilometre-scale regional climate modelling

Ella Gilbert[1], Denis Pishniak[2], José Abraham Torres[3], Andrew Orr[1], Michelle Maclennan[4], Nander Wever[5], Kristiina Verro[6]

[1] British Antarctic Survey, Madingley Road, Cambridge, UK.
[2] National Antarctic Science Centre of Ukraine, Kyiv, Ukraine.
[3] Danish Meteorological Institute, Copenhagen, Denmark.
[4] University of Colorado Boulder, Boulder CO, USA.
[5] WSL Institute for Snow and Avalanche Research SLF, Davos, Switzerland.
[6] Institute for Marine and Atmospheric Research, Utrecht University, Utrecht, Netherlands.

Correspondence to: Ella Gilbert (ellgil82@bas.ac.uk)

Abstract. We explore how atmospheric rivers (ARs) in a summer and winter case interact with the topography of the Amundsen Sea Embayment, West Antarctica, and deposit significant precipitation amounts. To do this we use results from three regional climate models (RCMs: MetUM, Polar-WRF, HCLIM) at a spatial resolution of 1 km. Estimates of snowfall associated with both events from all three RCM simulations compare well against observed snow height measurements over the Thwaites and Pine Island ice shelves. By contrast, snowfall estimates from ERA5 reanalysis for both events are severely underestimated (by 3-4 times) compared to the measurements. Outputs from the RCMs also show that the ARs may be associated with several millimeters of rain in both the summer and winter cases, although in the absence of *in situ* measurements of rainfall, this result cannot be directly verified. The RCM simulations suggest that rainfall during these events can fall directly as supercooled drizzle, but also that rainfall is concentrated around steep terrain due to the interaction of ARs with complex orography. We also show that while the amount of MetUM-simulated snowfall was comparatively resolution insensitive, the amount of rainfall simulated was not, with rainfall amounts over Thwaites ice shelf 4-16 times higher in 1 km simulations compared to 12 km simulations. Our work highlights that kilometer-scale models are useful tools to investigate the total precipitation amount and its partitioning into rain and snow over this globally important and climatically sensitive region, and the critical need for *in situ* observations of rainfall.

1 Introduction

West Antarctica, and particularly the Amundsen Sea Embayment (ASE), has been the focus of attention in recent years because of the rapid pace of climate and cryospheric change there. Glaciers in the ASE, and in particular the Thwaites (TG) and Pine Island (PIG) glaciers, have been highlighted because they are accelerating and losing ice mass extremely fast, largely due to basal melting (Lhermitte et al., 2020; Rignot et al., 2019). The ice shelves restraining TG and PIG have been shown to be

vulnerable to damage and weakening, and are changing very rapidly, thinning and retreating in response to oceanic and atmospheric warming (Lhermitte et al., 2020; Alley et al., 2021). In fact, over a third of the mass loss from West Antarctica comes from ice shelves (Smith et al., 2020).

The health of ice shelves can be partly measured by the surface mass balance (SMB). Ice shelf SMB describes how inputs of precipitation (accumulation) are balanced by losses of melt runoff, sublimation and evaporation (ablation). Snowfall accumulation is the primary counterbalance to dynamical and surface losses from ice shelves, with redistribution (e.g. via blowing snow) playing an additional role (Mottram et al. 2020; Lenaerts et al., 2019). Accumulation does not currently offset the aforementioned losses on ASE ice shelves (Rignot et al., 2019) but is vital to quantify because it can have an important effect on the timing and characteristics of ice shelf collapse, or recession and thinning (Scambos et al., 2017; Medley & Thomas, 2019; van Wessem et al., 2023). Antarctic accumulation is expected to increase as climate changes because a warmer atmosphere has a higher saturation vapour capacity as per the Clausius-Clapeyron relationship (Clausius, 1850; Clapeyron, 1834), meaning it can retain more moisture. However, increased precipitation will likely not balance increased losses over the 21st century (Gilbert & Kittel, 2021; Kittel et al., 2021).

Extreme precipitation events account for a large proportion of annual precipitation on the ASE coast, with 50% of annual precipitation falling in approximately 30 days per year (Turner et al., 2019). And they matter: Davison et al. (2023) demonstrate that extreme precipitation can play an important role in offsetting some of the notable mass losses in the ASE, and Wille et al. (2024) show that extreme precipitation in East Antarctica in March 2022 helped to make 2022's annual mass balance positive – a rare occurrence.

Moreover, atmospheric rivers (ARs) often coincide with extreme precipitation events in the ASE region and account for up to 11 % of annual precipitation totals, despite making landfall on just ~3 days per year (Wille et al., 2021, Maclennan et al., 2023). These long, filament-shaped atmospheric features transport large quantities of water vapour meridionally, and have been described as "rivers in the sky" that can greatly impact Antarctic precipitation variability (Shields et al., 2022). ARs are frequently associated with the presence of a high/low pressure couplet and blocking anti-cyclone that funnels warm and moist air towards the continent (Wille et al., 2019; Scott et al., 2019; Baiman et al., 2024). Adusumilli et al. (2021) showed that extreme precipitation events explained 41% of snow height changes over the West Antarctic ice sheet in 2019 and that the majority were associated with the infrequent but intense precipitation brought by ARs. However, Davison et al. (2023) note that 2019 and 2020 were both extreme precipitation years, implying that these results may not be representative.

The localised impacts of ARs in Antarctica have been shown to be extremely important. The characteristics of ARs in Antarctica differ from those elsewhere – for instance they make landfall less frequently and the colder polar atmosphere means they transport less moisture than at lower latitudes (Maclennan et al., 2023). They are also strongly impacted by the steep terrain of the Antarctic ice sheet, which often results in the coincidence of ARs with foehn events, raising temperatures and

wind speeds but causing a drying (Elvidge & Renfrew, 2016; Gilbert et al., 2022). This foehn + AR combination has previously been shown to be important over the Antarctic Peninsula (Bozkurt et al., 2018; Wille et al., 2022; Zou et al., 2023; Gorodetskaya et al., 2023) and South Orkney Islands (Lu et al., 2023). Francis et al. (2023) also show that foehn winds over PIG have a considerable impact on the ice shelf mass balance via their effect on sublimation and that these can be combined with ARs to induce considerable warming. But they can also impact precipitation, for instance Gehring et al. (2022) show how an AR and foehn event combined to affect precipitation phase and the quantity of snow reaching the ground at Davis, East Antarctica. That study also showed how the specifics of how the airflow interacts with steep topography can strongly influence precipitation phase, for example via the impact of foehn on the sublimation of precipitation particles.

ARs are also associated with the occurrence of rainfall over Antarctica (Wille et al., 2019, 2021, 2024; Lu et al., 2023). This is primarily due to warm air advection and moisture convergence facilitated by ARs, which elevate temperatures and increase the likelihood of liquid precipitation (Bromwich et al., 2024; Bozkurt et al., 2024). For example, ARs were responsible for approximately 30% of the rainfall recorded in the ASE between 1980-2018 (Wille et al., 2021) and were implicated in the record-breaking East Antarctic heatwave of March 2022, which resulted in rainfall over the periphery of the ice sheet and ice shelves (Wille et al., 2024). Vignon et al. (2021) show that rain falls up to 100 days per year at low elevation regions around the Antarctic coast, including over ice shelves. Rainfall is an important climate indicator but can also contribute to surface melting by the freezing of the liquid water within the snowpack releasing latent energy to the environment, as well as lowering the surface albedo (Doyle et al., 2015; Wille et al., 2021; Box et al., 2022; 2023). Rainfall also impacts firn properties by filling pore spaces and driving densification, and if it refreezes in the snowpack rain can form ice lenses that reduce the stability of ice shelves (Harper et al. 2023; Noël et al., 2023). The interaction of airflow with steep terrain can also impact the phase and characteristics of precipitation, for example enhancing rainfall production via the seeder-feeder mechanism (Lean & Clark, 2003) and generating supercooled drizzle in mixed-phase clouds (Fernandez-Gonzalez et al., 2015; Ramelli et al., 2021). Supecooled drizzle remains liquid at temperatures below the freezing point of 0°C. Seeder-feeder processes involve a higher-level cloud (the 'seeder') precipitating ice crystals into a lower cloud containing liquid droplets (the 'feeder') where they grow via riming or vapour deposition, thus enhancing liquid precipitation (He et al., 2022).

The quantity and characteristics of precipitation falling over ice shelves in the ASE are highly dependent on localised characteristics such as orography, which are not adequately represented by either sparse *in situ* observations or coarse resolution atmospheric reanalyses (Turner et al., 2019; Mottram et al., 2020; Gehring et al., 2022; Nicola et al., 2023). This constitutes a clear knowledge gap, which must be addressed to better estimate SMB and loss of mass from ice sheets (IPCC, 2019; Pritchard, 2021). Additionally, while several studies have used reanalysis to explore precipitation extremes associated with ARs over the ASE region (e.g. Francis et al., 2023; Maclennan et al., 2023; Wille et al., 2021), such datasets do not have sufficient resolution to explore the impact of complex orography on AR precipitation dynamics and characteristics. Using regional climate models (RCMs) to dynamically downscale reanalysis to high spatial and temporal resolution has been shown

to be critical to resolve the important fine-scale processes, interactions, and circulations that contribute to precipitation, including extremes (Gilbert et al., 2020; 2022; Morrison et al., 2020; Lu et al., 2023).

This study uses a mini-ensemble of three state-of-the-art kilometre-scale RCMs to explore the interactions between ARs and the TG and PIG ice shelves during two extreme precipitation events in winter and summer 2020. We aim to quantify the precipitation deposited during the ARs, including rain, which may affect the SMB and stability of these ice shelves. Additionally, we evaluate the performance of these RCMs in this region in capturing the dynamics of extreme precipitation in this climatically sensitive region, where observations are limited. By understanding the drivers and impacts of AR-induced extreme precipitation, this work seeks to determine the extent to which ice mass loss from important ice shelves and glaciers in the region can be modulated by accumulation.

2 Materials and methods

We use a mini-ensemble of three regional climate models (RCMs: MetUM, Polar-WRF and HCLIM) over the region centred on the PIG and TG ice shelves to simulate two extreme precipitation / AR case studies: a winter case (23-30 June 2020) and a summer case (3-9 February 2020), which is also used in Maclennan et al. (2023). We then compare simulation outputs with near-surface meteorological automatic weather station (AWS) data on the TG ice shelf, as well as accumulation data derived from observations of snow height at the station to provide a ground-truth of accumulated mass. We also include simulations by the SNOWPACK snow model (Wever, 2022), where the model derived accumulation and snow water equivalent are derived directly from the snow height sensor measurements (Maclennan et al., 2023). SNOWPACK allows a direct comparison of the observations against RCMs and ERA5 reanalysis (which output snow and rain mass quantities), and therefore provides a ground-truth of accumulated mass that enables us to evaluate precipitation phase partitioning. Further information regarding the RCMs is given in section 2.1, the ERA5 reanalysis is described in section 2.2, the details of the observational data are given in section 2.3, and the SNOWPACK firn model is described in section 2.4.

2.1 Regional Climate Models

All three RCMs use a one-way nesting approach to dynamically downscale ERA5 reanalysis (Hersbach et al., 2020, described in section 2.2) to very fine resolution (1 km horizontal grid spacing) with a series of intermediate nests. The MetUM and HCLIM use exactly the same domains, with the 1 km inner domain nested within an intermediate 3 km and 12 km domain, as shown in Figure 1a. Figure 1b shows the 1 km domain, which is focused on the region of interest. Meanwhile, Polar-WRF uses a setup focused on the same region but with a 9 km outer domain, and 3 km and 1 km domains with a larger areal extent, as shown in Figure S1. The RCMs all have a model top of approximately 40 km, with 52, 65 and 70 vertical levels in Polar-WRF, HCLIM and the MetUM, respectively, including 16, 20 and 14 levels below 1 km altitude. All three RCMs derive their model surface elevation and land/sea mask from updated high resolution datasets. For the MetUM and Polar-WRF this is the

REMA dataset at 200 m resolution (Howat et al., 2019), whereas for HCLIM this is v3 of the MEaSUREs BedMachine elevation model (Morlighem et al., 2022) at 500 m resolution.

The ERA5 reanalysis is used to supply the RCMs with initial and boundary conditions. We use standard atmospheric variables
130 to initialise the model (temperature, pressure, winds and humidity) as well as sea surface temperature and sea ice. For Polar-WRF and HCLIM, these conditions are applied directly to the edges of the outer nest (9 km and 12km, respectively). For the MetUM, ERA5 is used to force a global model configuration of the MetUM at approximately 40 km horizontal resolution, which then provides boundary conditions for the outermost 12 km nest of the MetUM. Both HCLIM and Polar-WRF are run continuously for each case with boundary conditions supplied at three-hourly intervals, and the first 24 hours of the model run
135 discarded as spin-up. The MetUM is run in 'forecast mode', which means it is re-initialised at 12-hourly intervals, and then run for 24-hour forecasts. The initial 12 hours of each forecast are discarded as spin-up, while the second halves are kept and concatenated into a continuous time series, as in Gilbert et al. (2022).

The following sub-sections describe relevant technical differences and parameterisations used in each model.
140
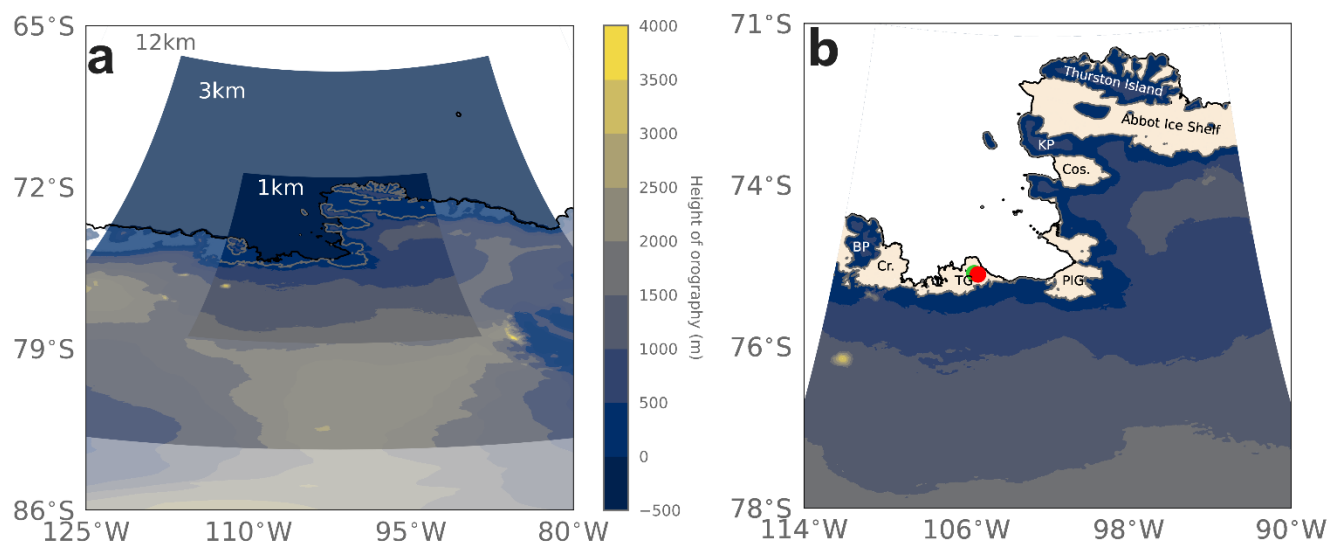
Figure 1. Model domains used in this study. Panel a) shows the mean height of REMA orography (Howat et al., 2019) over the 12 km, 3 km and 1 km domains, with ice shelf outlines shown in grey on the innermost 1 km domain. Panel b) shows the 1 km domain, with ice shelves shown in off-white and important locations labelled as follows: BP – Bear Peninsula, Cr. –
145 Crosson Ice Shelf, TG – Thwaites Glacier Ice Shelf, PIG – Pine Island Glacier Ice Shelf, Cos. – Cosgrove Ice Shelf, KP – King Peninsula, Abbot Ice Shelf, Thurston Island. The red and green circles show the location of the Channel and Cavity stations, respectively.

2.1.1 MetUM

The MetUM global model is run using the GA7 science configuration (Walters et al., 2019), while the nested domains are run

150   using the RA2M science configuration described in Bush et al. (2023). This means that convection is parameterised in the 12 km nest (according to the 5a scheme originally developed by Cullen, 1993), while it is explicitly resolved in the 3 km and 1 km domains. The formulation of the (diagnostic) large-scale cloud scheme used in RA2M is similar to the configuration described in Gilbert et al. (2020), including the modifications of Abel et al. (2017). These adaptations limit the overlap between cloud liquid and ice phases, thereby reducing the positive cloud ice and negative cloud liquid biases present in previous model

155   versions. The microphysics scheme is based on Wilson & Ballard (1999) with extensive modifications and represents five hydrometeors (cloud, ice, snow, rain and graupel). The single-moment scheme uses a fixed cloud droplet number and generic ice particle size distribution of Field et al. (2007). Further details of the scientific specification of RA2M can be found in Bush et al. (2021).

2.1.2 Polar-WRF

160   Polar-WRF vn (v4.1.1) is a version of the Advanced Research WRF core (Skamarock, 2019) modified to perform well in the polar regions (Xue et al., 2022). Cloud fraction is parameterised using the diagnostic scheme of Xu & Randall (1996). Convection is parameterised in the coarsest 9 km domain using the Kain-Fritsch scheme for deep and shallow convection (Kain, 2004), and explicitly resolved in the 3 km and 1 km domains. Precipitation and cloud microphysics are parameterised according to the scheme of Morrison et al. (2008), which is a double-moment scheme that represents four hydrometeors (ice,

165   snow, rain and graupel) and is suitable for cloud-resolving simulations. Further description of the physics configuration of Polar-WRF can be found in Hines et al. (2019), Bromwich et al. (2013) and Wilson et al. (2011).

2.1.3 HCLIM

HCLIM43–AROME (HCLIM in this study) uses a statistical large-scale cloud scheme based on Bechtold et al. (1995) to determine cloud fraction, and shallow convection is parameterised according to the eddy diffusivity mass-flux framework

170   (EDMFm; de Rooy and Siebesma, 2008; Bengtsson et al., 2017). Deep convection is explicitly resolved. A single-moment cloud microphysics scheme, ICE3 (Pinty and Jabouille, 1998; Lascaux et al., 2006), is used to parameterise precipitation, with modifications applied for cold conditions (OCND2; Müller et al., 2017). The scheme represents six species of water (vapour, cloud droplets, pristine ice, rain, snow/aggregates and frozen drops/graupel) and the OCND2 modifications separate fast liquid-phase processes from the slower cold-phase processes. A more detailed description of the HCLIM-AROME model system is

175   presented in Belušić et al. (2020).

2.2 ERA5 reanalysis

ERA5 is the latest reanalysis product from the European Centre for Medium Range Weather Forecasting (ECMWF), spanning the period 1940 to present. The production of ERA5 involves the assimilation of vast quantities of historical observations into the ECMWF's operational forecast model (IFS, at cycle 41r2), which outputs variables hourly on 137 vertical levels at ~31 km horizontal resolution. The model's surface orography is interpolated from numerous elevation datasets, including SRTM30, as described in ECMWF (2016). Its surface scheme, HTESSEL, represents surface fluxes, snow and SMB-relevant quantities like melt and runoff on surface tiles (Balsamo et al., 2009), while four cloud species (cloud liquid, ice, rain and snow) and fractional cloud cover are described prognostically by the precipitation and large-scale cloud schemes (ECMWF, 2016). Radiation is computed by the McRad scheme (Morcrette et al., 2008).

2.3 *In situ* data description

Observational data are taken from two instrumented stations on the eastern side of the TG ice shelf: Cavity Camp (75.033°S 105.617°W) and Channel Camp (75.050°S, 105.4334°W), situated approximately 4 km apart. Cavity Camp is located on a flat, relatively spatially homogeneous area of the ice shelf, whereas Channel Camp is located in the surface expression of a basal melt channel, which can be regions that preferentially develop surface crevasses (Alley et al., 2016; 2021). The Cavity and Channel stations are located approximately 20 km from the grounding line region of the TG ice stream where the terrain begins to slope steeply upwards. The stations are equipped with Automated Meteorology–Ice –Geophysics Observation System (AMIGOS) instruments, including sensors to measure near-surface meteorology like near-surface air temperature, relative humidity, pressure and wind speed, as well as firn temperature, snow height and GPS position at hourly resolution. A full description of the AMIGOS setup is given in Scambos et al. (2013).

2.4 SNOWPACK model

We also use output from simulations using the SNOWPACK multi-layer firn model (Wever, 2022) that were performed by Maclennan et al. (2023). In these simulations, the model is used to convert the observed snow height data from the AMIGOS instruments on the TG ice shelf to mass accumulation (Lehning et al., 2002a; 2002b). The SNOWPACK model calculates the surface energy balance based on the observed near-surface meteorological variables, including wind speed, temperature, relative humidity, and incoming short- and longwave radiation. It uses the surface energy balance to diagnose surface height changes from terms like surface melt and sublimation, and also calculates snow height decreases from compaction. Then, the calculated snow height is compared to the observed snow height to determine the accumulation terms. The model diagnoses snowfall when all three of the following conditions are met: observed snow height exceeds the simulated height, relative humidity exceeds 50%, and the difference between air and snow surface temperatures is less than 3°C (Lehning et al. 1999; Wever et al., 2015). Accumulated snow mass is calculated according to Schmucki et al. (2014) using the density of fresh snow, while describing the effect of snow erosion and deposition on snow density using the Redeposit scheme (Wever et al., 2023).

This approach provides time-varying new snow density, which, for this area, results in a calculated average surface snow density of approximately 450 kg m^{-3}. Rainfall is assumed when the air temperature exceeds 1.2°C, during periods where the forcing model predicts precipitation. In this study, we compare the local accumulation at the Cavity and Channel stations to modelled snowfall rates. However, it is important to note that the local accumulation can be substantially impacted by net snow erosion if the station is located in a region of drifting snow divergence, or by deposition when the station is in a zone of drifting snow convergence. Other sources of uncertainty concern the density of new snow, which can be in the order of 20-30% (Keenan et al., 2021), and which directly impacts the estimated accumulated mass from snow height measurements. Our approach also assumes that decreases in snow height are correctly captured by the model. Sublimation generally leads to very small changes in snow depth over the period of the described events andmelt during the events was also estimated to be too small to lead to any substantial surface height decrease. The snow depth measurements show a strong increase in snow depth, suggesting that any possible wind erosion of the snow surface was overshadowed by the net increase in mass in the area.

3 Results & Discussion

3.1 Case description Both the summer and winter cases examined in this work have a similar synoptic setup, with cross-terrain flow established by an atmospheric pressure dipole between the northwestern Antarctic Peninsula (high pressure) and Amundsen Sea (low pressure), as shown in Figure 2. This same synoptic setup is shown to be responsible for establishing cross-terrain flow and foehn winds over PIG and the wider ASE region (Francis et al., 2023). Both feature extreme precipitation, with SNOWPACK-simulated accumulation totals of 108 mm w.e. and 80 mm w.e. in summer at the Cavity and Channel stations, respectively and 61 mm w.e. and 113 mm w.e., respectively, during winter. In both cases, observations suggest that near-surface temperatures rose to the melting point of 0°C, supporting previous studies (e.g. Maclennan et al., 2023; Lu et al., 2023) that extreme precipitation events can have consequences not only for accumulation, but also for melting (see Figure S2). Both cases are also detected by the Wille et al. (2021) AR-detection algorithm (not shown).

The summertime case consists of a family of three ARs that made landfall over TG and the ASE coast in quick succession, driven by a high-low pressure couplet (Figure 2a). A pressure dipole, with low pressure over the Amundsen Sea (reaching a minimum MSLP value of 951 hPa in ERA5) and high pressure over the eastern tip of South America (maximum MSLP of up to 1035 hPa), drove convergence along a pressure ridge that extended lengthways along the eastern side of the Antarctic Peninsula. The high pressure system strengthened over the course of the case, enhancing the pressure gradient and driving more intensified convergence. This channelled moist air towards and across the West Antarctic coast, especially over the region of TG / PIG, and prevented the low pressure systems over the Amundsen Sea from migrating. The air mass picked up moisture as it travelled over the largely sea ice-free Bellingshausen Sea west of the peninsula and was forced over the topography of the West Antarctic Ice Sheet.

The wintertime case consists of high pressure over the Drake Passage and Bellingshausen Sea (top left of Figure 2b, with

240   ERA5 MSLP reaching up to 1035 hPa) and low pressure over the Amundsen Sea (bottom left of Figure 2b, with ERA5
MSLP falling as low as 955 hPa) (Figure 2b). A chain of low pressure systems pushed towards the ice sheet from sub-polar
latitudes all the way to approximately 85°S during the case, driving high temperatures and precipitation over the ASE
region.

245
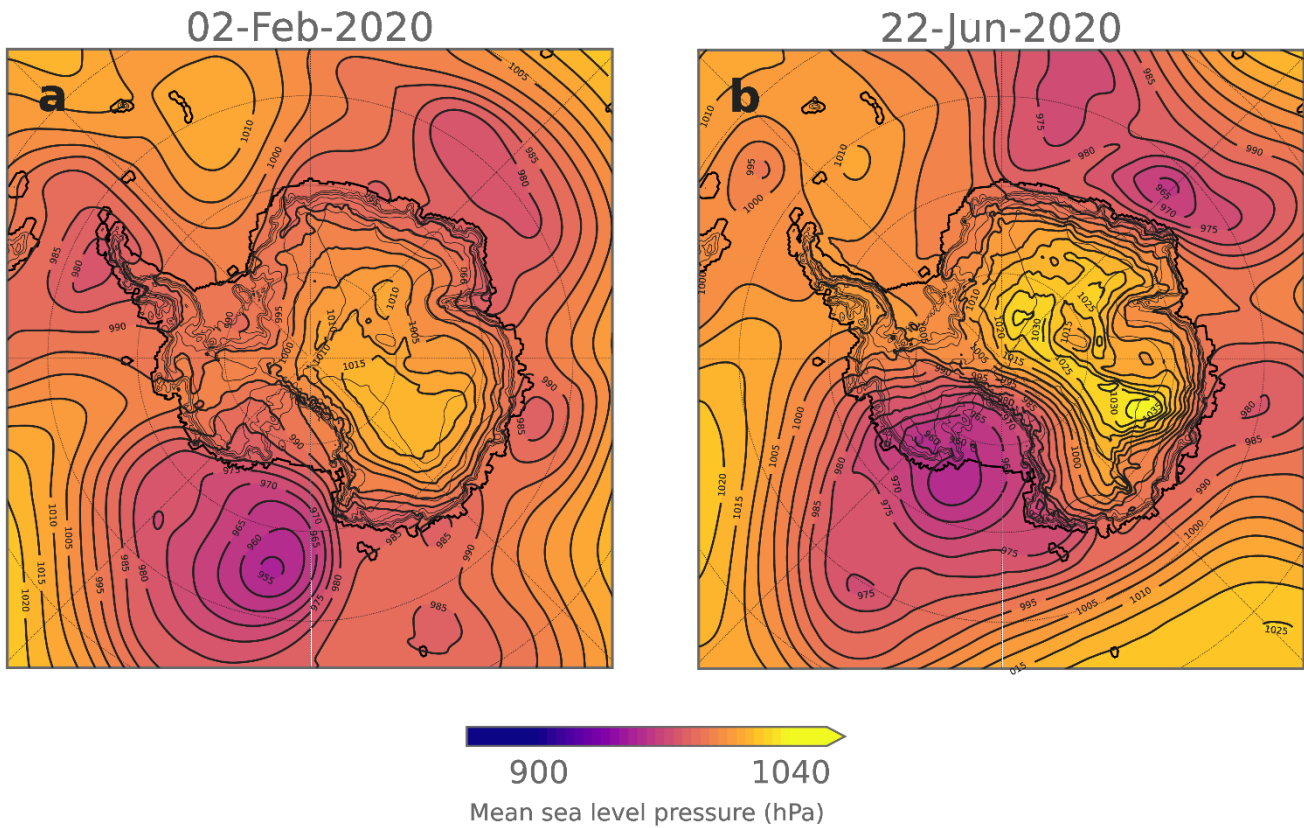
Figure 2. Mean sea level pressure at the onset of the summer (a) and winter (b) cases, from the ERA5 reanalysis. Contours
show mean sea level pressure in hPa, averaged over the first 24 hours of each case. Surface orography is also indicated by the
grey contours.

250

255 **Table 1.** Summary statistics for key variables over the Thwaites and Pine Island ice shelves during the summer and winter case studies, as simulated by the three RCMs. Multi-model means of ice shelf-averaged median and maximum values are shown, with the range of RCM values shown in brackets.

	Air temperature (°C)		Accumulated snow amount (mm w.e.)		Accumulated rain amount (mm w.e.)	
Summer	Median	Maximum	Median	Maximum	Median	Maximum
Thwaites	-0.33	2.61	46.50	77.82	10.90	40.06
	(-0.8 – 0.1)	(2.1 – 3.5)	(35.9– 55.1)	(50.0 – 96.4)	(2.5 – 16.9)	(13.2 –52.2)
Pine Island	0.06	5.70	15.54	49.18	13.51	50.0
	(-0.9 – 0.8)	(4.3 - 6.7)	(13.8-17.1)	(44.4 – 83.3)	(6.2 – 21.9)	(25.0 – 45.2)
Winter						
Thwaites	-12.12	-0.04	49.90	89.4	2.58	7.77
	(-13.3 to -10.6)	(-0.5 – 0.6)	(35.8-62.7)	(64.5-102.4)	(0.01 - 4.5)	(0.05 –15.8)
Pine Island	-10.75	1.62	20.13	53.91	0.71	6.00
	(-11.7 to - 10.2)	(1.3 – 1.9)	(10.1 – 30.8)	(44.4 – 63.9)	(0 – 1.1)	(0.8 – 8.7)

260

265

270

3.2 Precipitation

3.3.1 Time series of precipitation

The amount of snow and rain that falls over the PIG and TG ice shelves during the cases examined can tell us about the characteristics of extreme precipitation in the region. Here, we examine SNOWPACK-simulated total accumulation (shown as snow water equivalent, SWE), which comprises total precipitation minus losses via sublimation and runoff. We compare with precipitation amounts from ERA5 and the three RCMs. Figure 3 presents SNOWPACK-simulated SWE at the two stations alongside modelled (RCM + ERA5) ice-shelf average snowfall water equivalent amounts. An equivalent plot, which includes satellite-derived estimates of total precipitation, is shown in Figure S3. As shown in Figure 3a, summertime SNOWPACK-simulated SWE shows considerable differences between the two stations at Cavity and Channel, despite them being located just 4 km apart. In summer, higher overall SWE totals are simulated by SNOWPACK at Cavity than Channel, and SWE follows a different pattern at the two stations. As shown in Figure 3a, in terms of precipitation totals at Cavity, the first AR (3 February) is indistinguishable from the second (5 February): both bring a considerable amount of precipitation, driving steady and rapid accumulation between 3-6 February, followed by a pause and then another accumulation event associated with the third AR (8-9 February). This contrasts with the pattern for Channel shown in Figure 3a, which exhibits more modest overall accumulation totals and which increases in three distinct steps associated with each AR, with the first bringing relatively little snowfall in comparison to the second and third ARs in the sequence.

Reasons for the notable differences between SNOWPACK-simulated differences at Cavity and Channel could be localised geographic factors, the spatial characteristics of the ARs, or spatial heterogeneity in accumulation across the TG ice shelf. Firstly, the Channel Camp station is located in the surface expression of a basal melt channel which may experience higher rates of melting, and therefore lower calculated accumulation (Maclennan et al., 2023). Meanwhile, the Cavity Camp station is situated on a flat region of the TG eastern ice shelf. Secondly, the ARs each made landfall on slightly different parts of the TG ice shelf, with the first falling on the western side of the TG, the second progressing from west to east across TG, and the third hitting the eastern flank of TG (Maclennan et al., 2023). Additionally, the influence of extremely localised and topographically dependent processes such as blowing or drifting snow could have played a role in redistributing snow and therefore impacting accumulation at the two stations.

In the summer case, in comparison to SNOWPACK simulated accumulation, all RCMs under-estimate snowfall and do not capture the exact timing of the snowfall related to the ARs (Figure 3a), although this depends somewhat on the station considered. All three do better at Channel, with the MetUM and Polar-WRF simulating approximately the same amount of snowfall and HCLIM exhibiting lower amounts. The multi-model mean ice shelf median cumulative snowfall amount over TG ice shelf is 47 mm w.e. in the summer case (Table 2), which compares with SWE of 108 mm w.e. and 80 mm w.e. simulated by SNOWPACK at Cavity and Channel, respectively, making the multi-model mean RCM estimate of median

305 snowfall amount over TG ice shelf approximately two times smaller than the *in situ* observations suggest. Differences in simulated precipitation totals and the timing of precipitation events between the RCMs could be related to the way the models parameterise cloud microphysics or differences in their dynamics that determine how, when and where the simulated ARs make landfall. Meanwhile, the median cumulative ERA5-derived estimate of total precipitation over TG ice shelf in the summer case is even lower than the mean RCM estimate, at 28 mm w.e. (3-4 times lower than the SNOWPACK-derived

310 estimates), although still within the range of the RCM mini-ensemble (Figure 3a). This discrepancy is likely to be related to the coarser resolution of ERA5 and its orography, which would affect the passage and trajectory of airflow in the simulations, and hence the interactions between the AR and terrain. Convection is also parameterised in ERA5, which could produce different cloud dynamics and lower precipitation totals than the RCMs, which explicitly resolve convection at 1 km resolution.

315 In the winter case, a similar pattern is observed, with considerable differences between SNOWPACK-simulated snowfall between the Cavity and Channel stations and mismatches in terms of the timing of large snowfall deposits (Figure 3e). However, this time, it is the Channel station that has higher accumulation totals than Cavity. The multi-model mean ice shelf median cumulative snowfall amount over TG ice shelf is 50 mm w.e. in winter, compared with 61 mm w.e. and 116 mm w.e. simulated by SNOWPACK at Cavity and Channel, respectively (Table 2). This means the RCMs compare slightly more

320 favourably against observations in the winter case than in the summer case. Wintertime ERA5 values are again at the lower end of the range of RCM estimates over both ice shelves.

However, it must be noted that the snowfall/accumulation values shown in Figure 3 are not exactly comparable because the snow height sensor measurements used to drive SNOWPACK assume all positive height differences are related to snowfall

325 and processes that reduce accumulation, such as rain, melt, runoff, evaporation, wind-driven erosion or sublimation cannot be directly measured. As such, all these processes impact the observed snow height and SNOWPACK assumes that the effects of melt and sublimation are calculated correctly in its computation of the accumulation totals. As discussed in Section 2.4, the biggest sources of error in the SNOWPACK analysis probably come from the estimation of new snow density by the model, and the uncertainty related to blowing snow convergence or divergence. Based on our analysis, we expect that other,

330 negative, mass balance components were small during these events.
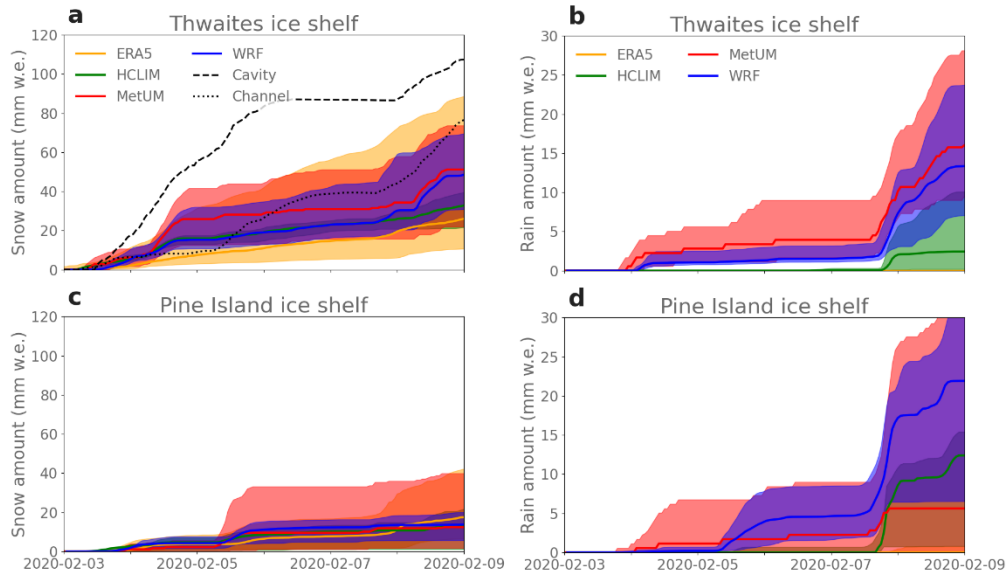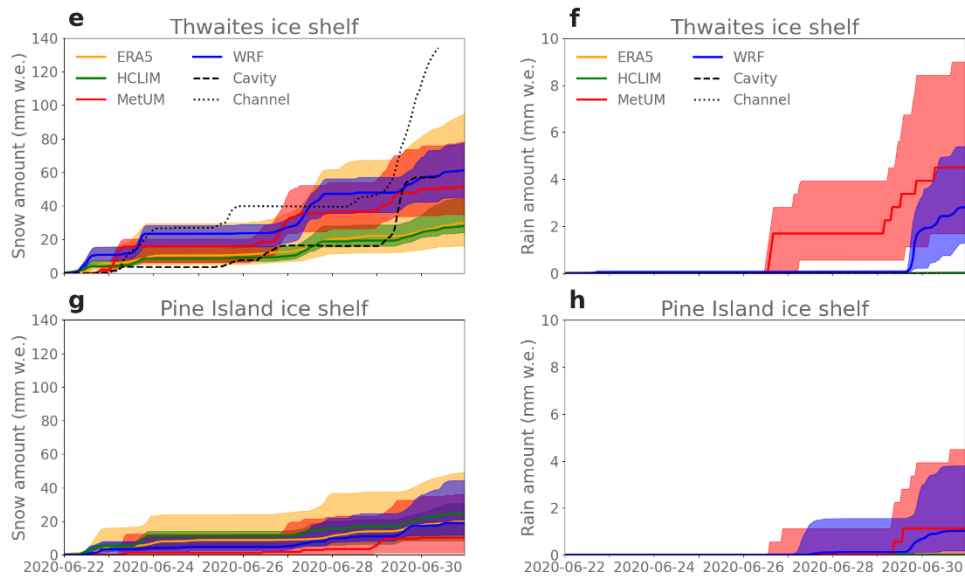
Figure 3. Time series of median snow (panels a,c,e,g) and rain (panels b,d,f,h) amounts (shown as water equivalent, in mm w.e.) during the summer case study on the Thwaites (a-d) and Pine Island (e-h) ice shelves. Median results from the 1 km MetUM, Polar-WRF and HCLIM domains are shown in red, blue and green, respectively, and ERA5 results are given in yellow. For all models, the shaded regions show the 5th to 95th percentile range of all values simulated across each ice shelf. SNOWPACK-simulated snow amounts derived from observations at the Cavity and Channel stations are shown in panel a) as the dashed and dotted black lines, respectively. Data are only shown until 0900 on 30 June 2020 in panel e due to instrument malfunction after this point. Note the different scales between summer and winter, and between snow and rain.

340 We also compared the ERA5, RCM and SNOWPACK-simulated totals with the GPM IMERG satellite product (see text S2 for further details). However, due to the product's limitations over snow and ice-covered surfaces, as well as its reliance on reanalysis data, we chose not to include it here. A figure comparing the satellite estimates to the model outputs shown in Figure 3 is given in Figure S3. It shows that during both cases, the satellite-derived estimates of total precipitation are extremely close to ERA5 (reaching median values of 28 mm w.e and 19 mm w.e. over the TG and PIG ice shelves in summer),

345 and considerably lower than the RCM and SNOWPACK estimates. The similarity to ERA5 is expected because the precipitation product is partly generated using reanalysis data that has assimilated the same observations as ERA5, and ERA5 also assimilates satellite data. The lower precipitation estimates derived from satellite data, as compared to the multi-model mean of the RCM estimates, is likely related to the lower resolution of the satellite product ($0.1° \times 0.1°$ or approximately 12 km) and may also reflect the difficulty of satellite sensors in measuring precipitation over cold snow and ice surfaces. This

350 underlines the challenges associated with evaluating precipitation extremes in Antarctica and reinforces the merit of high-resolution RCMs.

Neither ERA5 nor the satellite measurements shown in Figure S3 appear capable of capturing the spatial variability over the TG ice shelf that is implied by the large differences between the Channel and Cavity observations shown in Figure 3a and

355 Figure 3e. SNOWPACK-simulated accumulation at Channel in Figure 3a and at both stations in Figure 3e is mostly within the 5-95th percentile range of the RCMs and ERA5, but values at Cavity in summer and at Channel at the end of the winter case are well outside the modelled range, indicating that despite their high resolution, the RCMs still under-estimate snowfall amounts compared to *in situ* observations. The RCM 5th-95th percentile range demonstrates that the RCMs can capture the magnitude of spatial heterogeneity implied by the differences between Cavity and Channel. However, the time series at grid

360 points corresponding to each station's location (not shown) are extremely similar, suggesting that there are still unresolved spatial variations below the 1 km grid scale of the RCMs, or processes that are incorrectly represented. This may be partly because there are important processes that are unresolved in the RCMs, such as blowing or drifting snow, or because of deficiencies in important parameterisations such as cloud microphysics. Furthermore, small-scale variations in orography can cause blowing or drifting snow to accumulate in some locations preferentially, while the scale of localised and rapidly

365 evolving depressions or topographic features is below the grid scale of the models and may not be included in the datasets used to produce static boundary conditions such as surface altitude. The spatial variability of snow and rainfall over the domain is explored in greater detail in section 3.3.3 below.

However, it must be noted that the difference between RCM and SNOWPACK snowfall totals, particularly in the summer

370 case, is of approximately the same order of magnitude as the amount of rain simulated by the RCMs. This indicates that phase partitioning could be one of the main causes of the discrepancy between RCM-simulated and SNOWPACK-simulated snowfall. This may be because SNOWPACK uses a fairly simplistic temperature threshold to diagnose rain, based on when ERA5 2 m temperature reaches 1.2°C. As shown in Table *2*, the RCMs exhibit much warmer conditions over the TG ice shelf

than ERA5, suggesting that rain would have been diagnosed much less frequently based on ERA5 temperatures than the
RCM temperatures. Therefore it is possible that SNOWPACK underestimates rainfall: a conclusion also supported by the
fact that all three RCMs simulate summertime rain and that two of the three simulate rain in winter. Sensitivity experiments
(not shown) where the diagnostic threshold was varied between -2°C and + 2°C showed that in the summer case, lower
thresholds resulted in considerably higher SNOWPACK-derived rainfall totals. However, during winter and the threshold
needed to be lowered to considerably below zero to prognose rainfall. Note that when SNOWPACK diagnoses rainfall, this
is additional to the accumulation derived from snow depth measurements, and calculated accumulation is unchanged.

3.3.2 Precipitation phase

We next examine the phase partitioning of precipitation in the RCMs over the TG and PIG ice shelves during both cases.
During both cases, considerably more snow falls over the TG ice shelf than the PIG ice shelf in all models, with median
snowfall totals on average approximately 2-3 times higher over the TG ice shelf than the PIG ice shelf (Table 1). Meanwhile,
more rain falls over the PIG ice shelf in the summer case than the TG ice shelf, whereas in the winter case the TG ice shelf is
rainier (Table 1).

Table 2 shows that two out of three RCMs simulate rain in winter, with 0.01 – 4.5 mm w.e. falling over the TG ice shelf and up
to 1.1 mm w.e. over the PIG ice shelf in winter. Polar-WRF and the MetUM both simulate upwards of 1 mm w.e. in winter,
while HCLIM simulates negligible amounts. Further, all three RCMs simulate rainfall in summer, with 2.5 – 16.9 mm w.e. rain
falling over the TG ice shelf and 3.1 – 12.4 mm w.e. falling over the PIG ice shelf. The RCMs simulate the most rain at the end
of the summer case, particularly on the 7/8th February. However, the raw output from the snow height sensors on TG ice shelf
(Figure 4) indicates a period of accumulation during this timeframe (accumulating ~11 mm), which appears incompatible with
considerable rainfall. Typically, rain reduces the height of the snowpack by compacting snow (Marshall et al., 1999), which
means that significant rainfall is unlikely on the 8th February. However, there may be several explanations for this apparent
inconsistency between the observations and model results.

The time series shown in Figures 3a and 3b indicate that there were two periods of intense precipitation over TG ice shelf at the
end of the summer case: first from 1800 on 7 February until 0000 8 February, and then from around 0600 until 1800 on 8
February. During that first 6-hour window, the RCMs simulate minimal snowfall and relatively significant rainfall amounts: 6-
7 mm w.e. in Polar-WRF and the MetUM, compared with 2-3 mm w.e. snowfall (Figure 3a, b). However, during the second 12-
hour window, both snow and rain are simulated, with the MetUM and Polar-WRF simulating around 15 mm w.e. of snowfall,
compared with 5-6 mm w.e. rainfall. Given that the near-surface atmospheric conditions during this case were near the melting
point (see Figures 6 and S2), with warm air overlying the snowpack and observed 2 m temperatures fluctuating between -2°C
and +2°C, it is likely that precipitation was mixed phase. As a result, it is plausible that snow, rain and wet solid precipitation
such as wet snow or sleet all fell during this time. However, the RCMs used in this study have a relatively simplistic

categorisation of hydrometeors: the MetUM represents five while Polar-WRF represents four (HCLIM does not simulate considerable rain or snow during this period). Therefore, wet solid precipitation may have been classified as 'rain' in the RCMs, increasing the amount of rainfall simulated. As long as the amount of snow falling was comparatively greater than the amount

410 of liquid precipitation, the height of the snowpack could still have increased, but the amount of rain by mass would have been small. However, without a ground-truthing of rainfall from *in situ* measurements, it is difficult to say for certain whether rain indeed fell during these days.
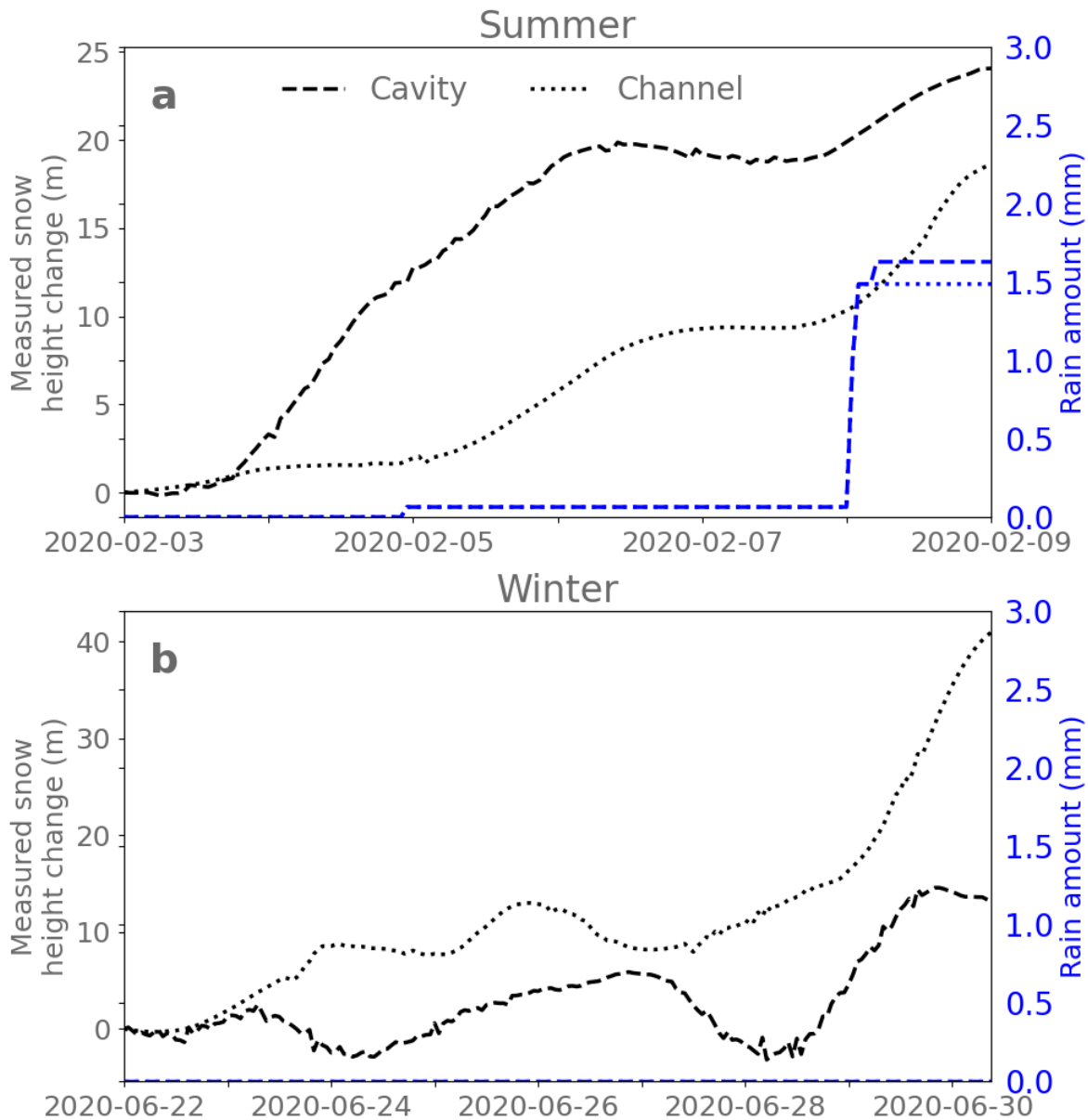
Figure 4. Smoothed measured snow height and SNOWPACK-simulated cumulative rainfall amounts in the summer (a) and winter (b) cases. Plots show measured snow height change (in m) in black and rainfall amounts (in mm) in blue. Both the Cavity and Channel stations are shown.

Considering the entire summer case, it seems plausible that a small amount of rain did fall. Indeed, this is supported by the SNOWPACK output, which indicates that 1.5 and 1.6 mm fell at Channel and Cavity, respectively, during the summer case,

420 including 0.9 mm w.e. at 0000-0600 UTC on the 8th February at both stations (Figure 4). The RCMs may have simulated rainfall at the wrong time or misclassified wet solid precipitation as rain. Further, as discussed above, the simple, ERA5-derived temperature threshold used to diagnose rain could cause SNOWPACK to underestimate rainfall compared to the RCMs. Additionally, any rain that fell at sub-zero temperatures (i.e. supercooled rain) would not be captured using this 1.2°C threshold. The same explanations probably apply to simulated winter rainfall too, although winter rainfall totals are much smaller in

425 comparison to snowfall and compared to the summer case. The caveat is that there are no *in situ* observations of rainfall to provide a ground-truthing of this result. However, the fact that rain is simulated by all three RCMs strengthens the notion that rain could indeed be falling during these extreme events and emphasises the need for *in situ* measurements of liquid as well as solid precipitation in West Antarctica.

3.3.3 Spatial variability of precipitation

430 The spatial variability of accumulated precipitation over the entire ASE region is also important. Figure 5 shows maps of accumulated snow and rain in ERA5 and the three RCMs during the two cases. In summer, the largest quantities of snow are simulated in the west of the domain (bottom right of all panels in Figure 5a-d), and along the windward slopes of the steepest terrain, for example the sloping topography on either side of the Abbot ice shelf, and the upwind slopes above the PIG and TG ice shelves. The total magnitude of accumulated snowfall is comparable between all three RCMs and ERA5, with the

435 MetUM and Polar-WRF standing out as the snowier models. A similar pattern is clear during winter (Figure S4). Figure 5e-h shows that rain also falls in the vicinity of steep terrain, but unlike snow, rain appears more confined to lower elevations.

Figure 3b, d and Figure 5 both show that all the RCMs simulate rainfall over the TG ice shelf and PIG ice shelf during summer, while ERA5 simulates rainfall over the PIG ice shelf only. During the summer case, an RCM median of 11 mm w.e.

440 (2.5 - 17 mm w.e.) rain falls over the TG ice shelf, while 13.5 mm w.e. (6 - 22 mm w.e.) falls over the PIG ice shelf (Table 1). Polar-WRF has relatively higher median rainfall totals over the PIG ice shelf than the MetUM and HCLIM (Figure 3d), but if we consider the spatial distribution of accumulated rainfall shown in Figure 5, the MetUM and Polar-WRF are extremely similar in terms of cumulative rainfall amounts. However, rain is simulated in different locations between the two models, with Polar-WRF simulating higher quantities of rainfall over the steepest terrain of Thurston Island on the northwestern

445 boundary of the Abbot Ice Shelf and more extensive rainfall over the PIG ice shelf. Meanwhile, the MetUM simulates pockets of higher rainfall near the windward side of steep terrain, including at the edge of the PIG and TG ice shelves where the terrain begins to slope upwards more steeply. HCLIM also simulates pockets of rainfall clustered near steep topography, particularly on Thurston Island and over the PIG ice shelf, but comparatively lower accumulated totals than in the other two RCMs. ERA5 accumulated rainfall totals are highest along the steep periphery of Thurston Island and the southwestern edge

450 of the PIG ice shelf, but overall much lower than all three RCMs.

The same pattern is observed in winter, with the MetUM and Polar-WRF simulating larger quantities of rainfall than ERA5 or HCLIM, but in contrast to the summer case, the MetUM stands out as the rainier model, simulating a band of rain of up to 30 mm w.e. along the spine of the steep topography of Thurston Island (Figure S4). More rain is simulated by all three RCMs during the summer case, because temperatures are higher and more precipitation falls in general. However, two out of three simulate modest quantities of rain during the winter case, which may indicate that even in winter liquid precipitation can still occur during the most extreme AR conditions. The differences between the RCMs in terms of the spatial distribution of rainfall and its intensity may be related to many factors, including the exact trajectory of the simulated ARs, temperature, moisture availability, model orographic interactions and cloud microphysics.

460

Table 2. Median air temperature in degrees celsius and median accumulated total snow and rainfall amounts in mm water equivalent (mm w.e.) for each model and ERA5 over the Thwaites and Pine Island Glacier ice shelves in the summer and winter cases.

	Thwaites			PIG		
Summer	Air temperature (°C)	Snow (mm w.e.)	Rain (mm w.e.)	Air temperature (°C)	Snow (mm w.e.)	Rain (mm w.e.)
MetUM	-0.3	55.1	16.9	0.3	15.8	6.2
WRF	0.1	48.5	13.4	0.8	13.8	21.9
HCLIM	-0.8	35.9	2.5	-0.9	17.1	12.4
ERA5	-10.7	27.9	<0.1	-11.8	18.9	<0.1
Winter						
MetUM	-12.4	51.2	4.5	-11.8	10.1	1.1
WRF	-13.3	62.7	3.2	-10.2	19.5	1.0
HCLIM	-10.6	35.8	<0.1	-10.3	30.8	<0.1
ERA5	-21.1	29.8	0.0	-21.6	19.9	0.0

465

The following sections will explore the origins and physical processes leading to the production of liquid precipitation during the extreme events simulated.
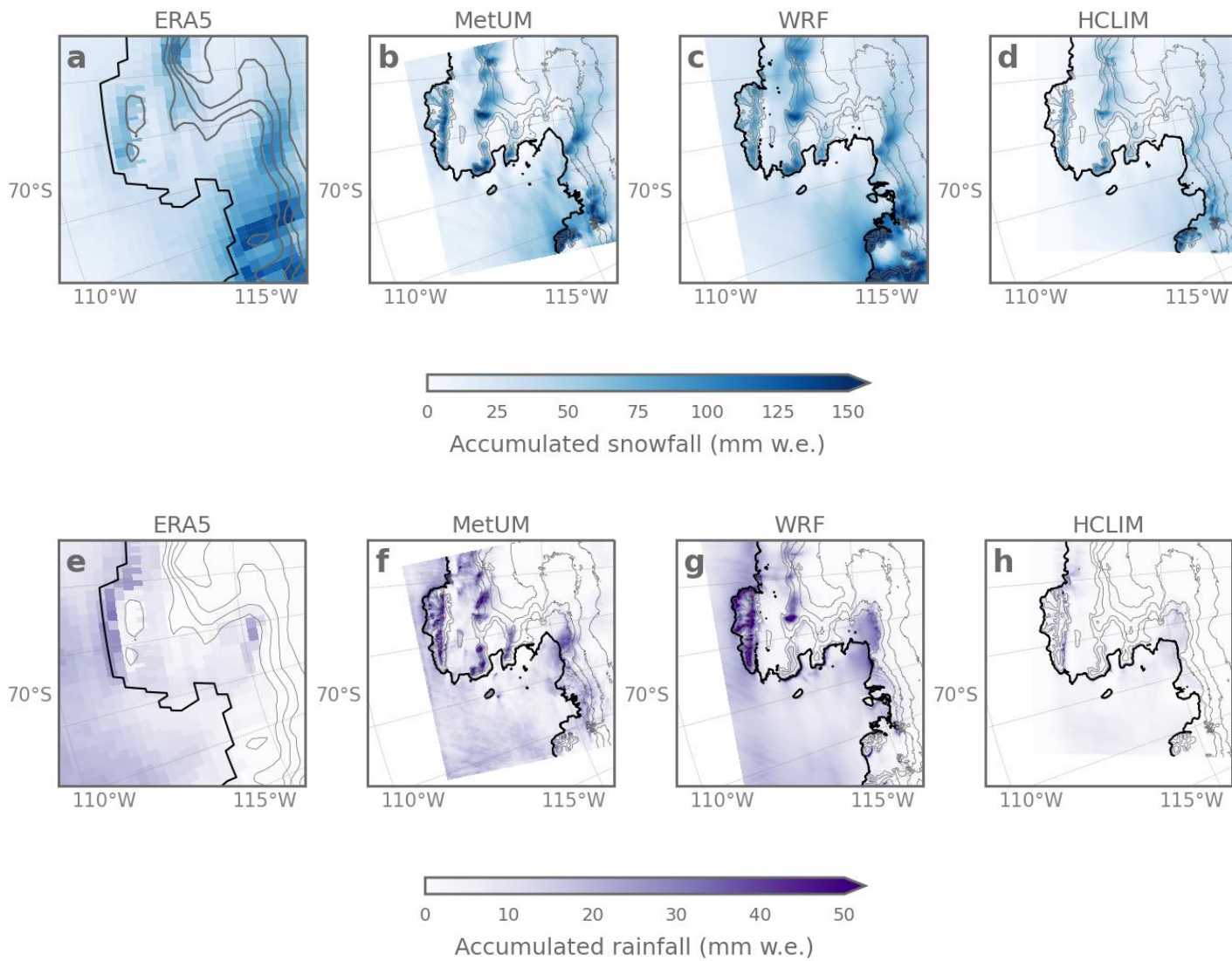
Figure 5. Accumulated total snow (panels a-d) and rain (panels e-h) during the summer case (3-9 February 2020), as simulated by ERA5, the MetUM, Polar-WRF and HCLIM at 1km resolution. An equivalent figure for winter is shown in Figure S4.

3.4 Origins of liquid precipitation in ARs

470 We have established that liquid precipitation is likely falling during the cases examined over the TG and PIG ice shelves. Next, we explore the origins of this rainfall. To avoid repetition, the following analysis will use data from the 1 km MetUM simulation only, which exhibits some of the highest rainfall totals.

Figure 6 shows the relationship between maximum air temperatures and accumulated rainfall totals during the winter and
475 summer cases in the MetUM. Maximum temperatures reach well above freezing at the lowest elevations in summer, especially over the PIG ice shelf, where maximum temperatures of ~5°C are simulated across much of the ice shelf nearest the surface (Figure 6a). However, maximum temperatures above zero are also simulated during winter over the Abbot, Cosgrove and PIG ice shelves (Figure 6d). These above-freezing temperatures are simulated over regions in the immediate lee of steep terrain, suggesting that a foehn effect could be altering the meteorology associated with the ARs, as also shown by Francis et al. (2023)
480 over PIG, by Gehring et al. (2022) over Davis, by Wille et al. (2022) over the Antarctic Peninsula and Lu et al. (2023) over the South Orkney Islands. A foehn effect could be expected to produce a warm pool near the surface in the lee of steep terrain when air flow is across this topography.

Panels b and c of Figure 6 show that there is indeed a warm pool of air at the surface over the TG and PIG ice shelves, and
485 that the region of above-freezing summer maximum mean air temperatures along the transects through TG and PIG reaches up to above 1 km in altitude, and up to nearly 2 km altitude over PIG. These higher temperatures aloft may be partly associated with a foehn effect, and/or by the air mass being orographically lifted, resulting in cooling, condensation and latent heating of the surrounding atmosphere. In winter, regions of above-zero maximum air temperatures are much more spatially confined and are concentrated in small pockets over the PIG ice shelf at altitudes below 750 m (Figure 6e), while temperatures remain
490 below freezing along the TG transect (Figure 6f).

Although near-surface temperatures over the PIG and TG ice shelves reach maximum values near or above freezing during both cases (Table 1, Figure 6), median temperatures are colder, remaining below freezing during the winter case and staying very close to zero in the summer case (Table 1). Further, most of the liquid precipitation falls at times and altitudes when
495 ambient temperatures are not above freezing, suggesting that temperatures above 0°C are not always required to produce rainfall.

Indeed, the highest rainfall totals over both the TG and PIG ice shelves are simulated at times and altitudes where temperatures are within a few degrees of 0°C. During the summer case, a near-surface warm pool develops each time the
500 three ARs push air over the steep terrain, particularly over the Abbot, Cosgrove and PIG ice shelves. When near-surface temperatures are highest (>2°C) and the surface warm pool is more vertically extended, rainfall totals are lower, suggesting

that the highest temperatures can reduce the amount of liquid precipitation via evaporation and/or sublimation. However, during times when maximum air temperatures reduce to more moderate values of around -2 to +2°C, rainfall totals become considerable over both the TG and PIG ice shelves. For example, rainfall totals over the TG ice shelf are highest during

505 easterly flow, which advects warm air from regions with the strongest foehn warming, allowing it to mix and cool by the time it reaches TG. Similarly, the highest rainfall totals over PIG are simulated when the warm pool begins to fade. Over both ice shelves, the highest rainfall totals are simulated along the flanks of steep terrain and often at altitudes 500-1500 m above the surface. During the winter case temperatures are cooler, so rainfall only occurs in periods of the strongest foehn warming. However, temperatures during these periods are also within the same range of -2 to +2°C.

510

The dashed lines in Figure 6 indicate the maximum height of the 0°C air temperature threshold and can be considered a maximum 'melt line' height. Below this threshold, snow and ice might be expected to melt and fall as rain if the melt layer that solid particles fall through is thick enough. However, in the summer case, the highest accumulated rainfall totals are not always concentrated below the melt line, especially in the case of the TG transect. Moreover, in the winter case the

515 region of above-zero temperatures is extremely spatially constrained along the PIG transect and completely absent along the TG transect. Despite this, accumulated rainfall totals in excess of 10 mm w.e. are simulated along the transects through both ice shelves, resulting in median summer surface rainfall totals of 16.9 mm w.e. and 6.2 mm w.e. over the TG and PIG ice shelves, respectively, and 4.5 mm w.e. and 1.1 mm w.e., respectively, in winter (Table 2). This means that supercooled liquid precipitation is falling, even fairly high up in the atmosphere.

520

Over both ice shelves and in summer especially, accumulated rainfall totals are higher just above the surface than at the surface, indicating that some rain is being lost to evaporation, riming or freezing as it descends through the warm near-surface layer, or that rain droplets are being lofted upwards by updrafts as air is forced to flow up the steep terrain of the ice stream, as described in Silber et al. (2019). Meanwhile in winter, most of the rainfall that reaches the surface is spatially

525 constrained to further along the TG transect, upstream of the grounding zone where the AR intersects with steep topography. Over the PIG ice shelf winter rainfall is more minimal, despite temperatures being warmer than over the TG ice shelf, as indicated in Tables 1 & 2.
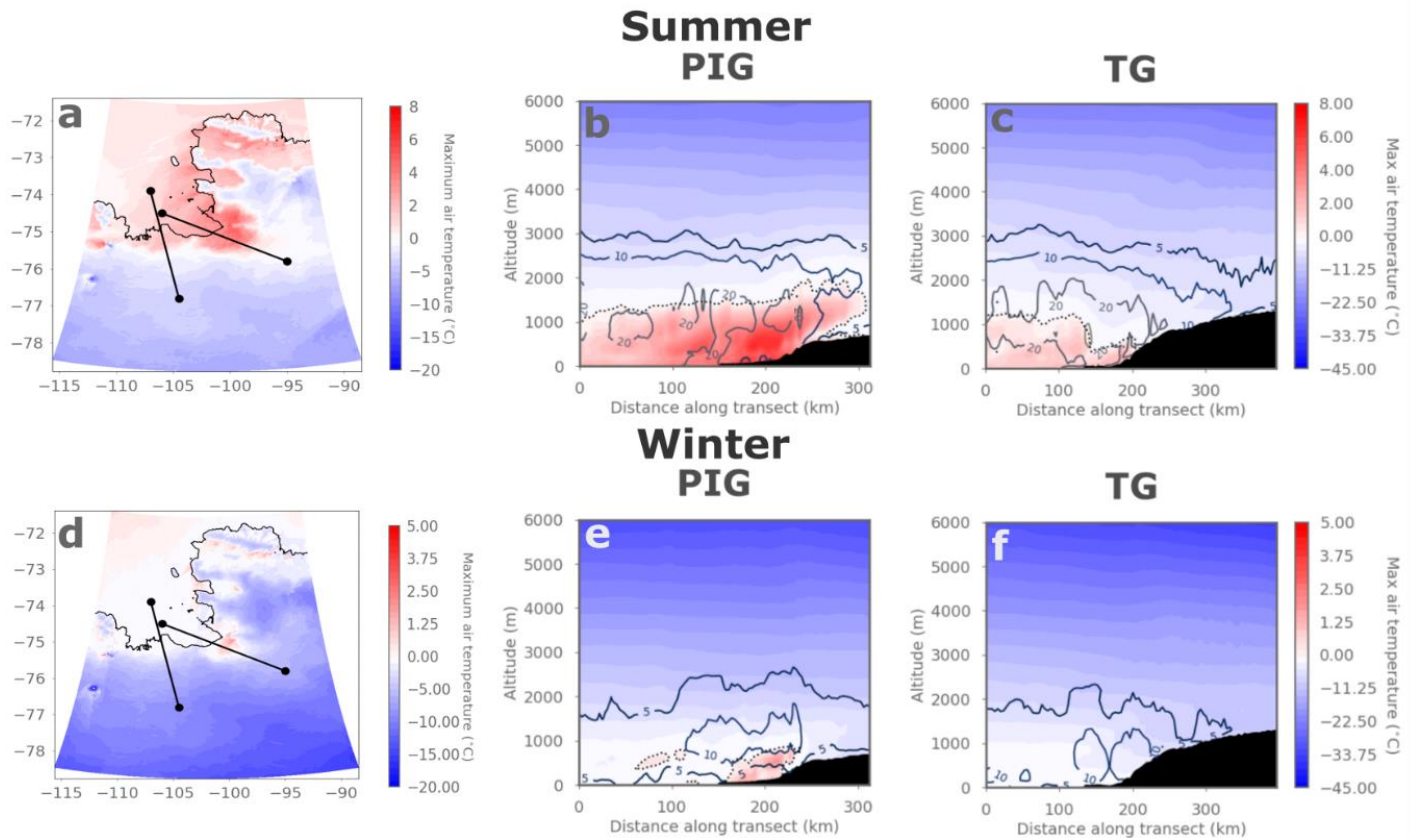
Figure 6. Characteristics of maximum air temperature and accumulated rainfall during the summer case (3-9 February 2020, top row) and the winter case (23-30 June 2020, bottom row). Panels a and d show maximum 1.5 m air temperature during each case, with the locations of the PIG and Thwaites transects indicated on the map. Panels b and e show transects of maximum temperature (colours) and accumulated total rainfall in mm w.e. (contours) across the Thwaites transect and panels c and f show the same across the PIG transect. In all transect panels, the dashed line indicates the maximum height of the 0°C air temperature threshold, and in all panels, red colours indicate maximum air temperatures above 0°C, while blue colours indicate temperatures colder than this threshold.

530

As shown in Figure 6, patterns of accumulated rainfall are relatively consistent between locations and seasons. In both seasons, rain is present at altitudes of up to ~2500 m, although in summer, the height of the 5 mm w.e. accumulated rainfall contour is marginally higher, reaching up to around 3000 m a.s.l. (Figure 6b, c). This is despite the patterns of maximum air temperature being quite different between the transects. In both seasons, there are also pockets of high accumulated

535   snowfall totals above the surface over the ice shelves (Figure S5), indicating that in some locations snow is sublimating and/or melting into rain as it descends through the warm layer described above. This same effect (snow transitioning to rain

as it falls through a warm layer) has been observed during combined AR / foehn conditions at Davis station in East Antarctica by Gehring et al. (2022).

540 Liquid precipitation falls from liquid-bearing mixed phase cloud at temperatures as cold as -11°C and -8°C in winter and summer, respectively (not shown), suggesting that the formation mechanisms are supercooled warm-rain processes. Cloud droplets reach a large enough size to descend through the atmosphere, collecting other droplets on their way and producing supercooled rain through warm-rain processes like collision-coalescence and accretion. Supercooled drizzle usually forms when there are insufficient ice nuclei to allow the atmospherically available water vapour to nucleate and grow into solid

545 precipitation via ice processes. This is also consistent with a pristine region such as the West Antarctic, and the northeasterly wind direction which has advected air from across Ellsworth Land where it is unlikely to have picked up ice nucleating particles. These results also suggest that rainfall is being generated via the seeder-feeder mechanism, which increases orographic rainfall rates, and can often result in the formation of supercooled drizzle in mixed-phase clouds (Fernandez-Gonzalez et al., 2015; Ramelli et al., 2021). The process involves ice or liquid descending from upper (seeder) levels and

550 enhancing the rate of accretion in lower (feeder) levels, thereby increasing surface rainfall amounts (Lean & Clark, 2003). It frequently occurs in regions with significant updrafts, such as when air is forced up and over steep terrain (Ramelli et al., 2021). Finlon et al. (2020) show that the 0°C isotherm separates the seeder and feeder levels in such cases, for example in an AR over the Southern Ocean, which is consistent with the results shown here.

555 In both cases, the region of accumulated rainfall reaches several hundred kilometres inland. Maximum air temperatures are higher over the PIG transect as shown in Figure 6a, but in summer, higher accumulated rainfall totals are simulated over the TG ice shelf and upstream (Figure 6b). This suggests that air temperatures are not the only control on rainfall totals, and that factors like large-scale cloud and synoptic patterns, as well as orography, likely influence the phase and quantity of precipitation that falls. Bromwich et al. (2024) and Bozkurt et al. (2024) also highlight the complexity of processes involved

560 in initiating the phase transition from snow to rain in ARs.

This is also supported by Figure 7, which shows the ratio of rain to snow over the TG and PIG transects in summer and hints at different formation mechanisms of precipitation. Hatched regions in Figure 7a show that there are several regions where the amount of summertime rainfall exceeds the amount of snowfall: most of these regions are offshore, with some

565 also immediately above the steepest slopes in the lee of airflow over the terrain, for example over the PIG and Abbot ice shelves. Along the TG and PIG transects shown in panels b and c, summer precipitation is largely mixed phase and accumulated totals are dominated by snowfall, but rain/snow ratios of above 0.5 (indicating that at least 33% of precipitation is falling as rain) highlight regions where rainfall totals are relatively high and liquid precipitation processes may be comparatively more important. Figure 7b shows that along the TG transect, the highest rain/snow ratio is found above the

570   zero-degree line at higher elevations around 150 km inland above the glacier slope. However at the surface, the highest rain/snow ratios are simulated at the foot of the steep terrain, as indicated by Figure 7d.

Along the PIG transect, much more snow falls relative to rain (Figure 7c), except at the lowest elevations and directly above the steepest orographic gradient (Figure 7e), where the effect of foehn-driven warming is highest (Figure 6a, b). Over the

575   PIG transect, the highest rain/snow ratios are found in the warmest regions, indicating that some of the rain has formed by the melting of solid precipitation as it descends through the warm near-surface layer (Figure 6c). Some of the precipitation likely also sublimates and evaporates as it descends through this warm layer, which is illustrated by the fact that the highest rainfall fluxes are simulated in pockets above the surface in both winter and summer.

580   The importance of super-cooled rain formation processes is especially evident in the winter case, where maximum air temperatures above 0°C are simulated only in extremely confined locations over the PIG ice shelf (Figure e). Supercooled liquid precipitation of up to more than 10 mm w.e. occurs over both ice shelves, especially at higher altitudes. This compares with maximum cumulative totals of ~20 mm w.e. in summer, i.e. double the magnitude of winter.

585   Liquid precipitation has been shown to occur at very low temperatures in Antarctica. For example, Silber et al. (2019) demonstrated that drizzle can occur at temperatures down to -25°C near McMurdo. They showed that in the presence of sufficient condensate, liquid precipitation can fall from stratiform clouds like those that were present during the summer case. In the cases studied here, the source of condensate was from the three ARRs that made landfall, as well as the orographic lifting and condensation of moisture in the air as it was forced over the steep topography. In the pristine Antarctic

590   atmosphere there are also fewer aerosols that can act as ice nucleating particles, thus preventing the rapid glaciation of the cloud.
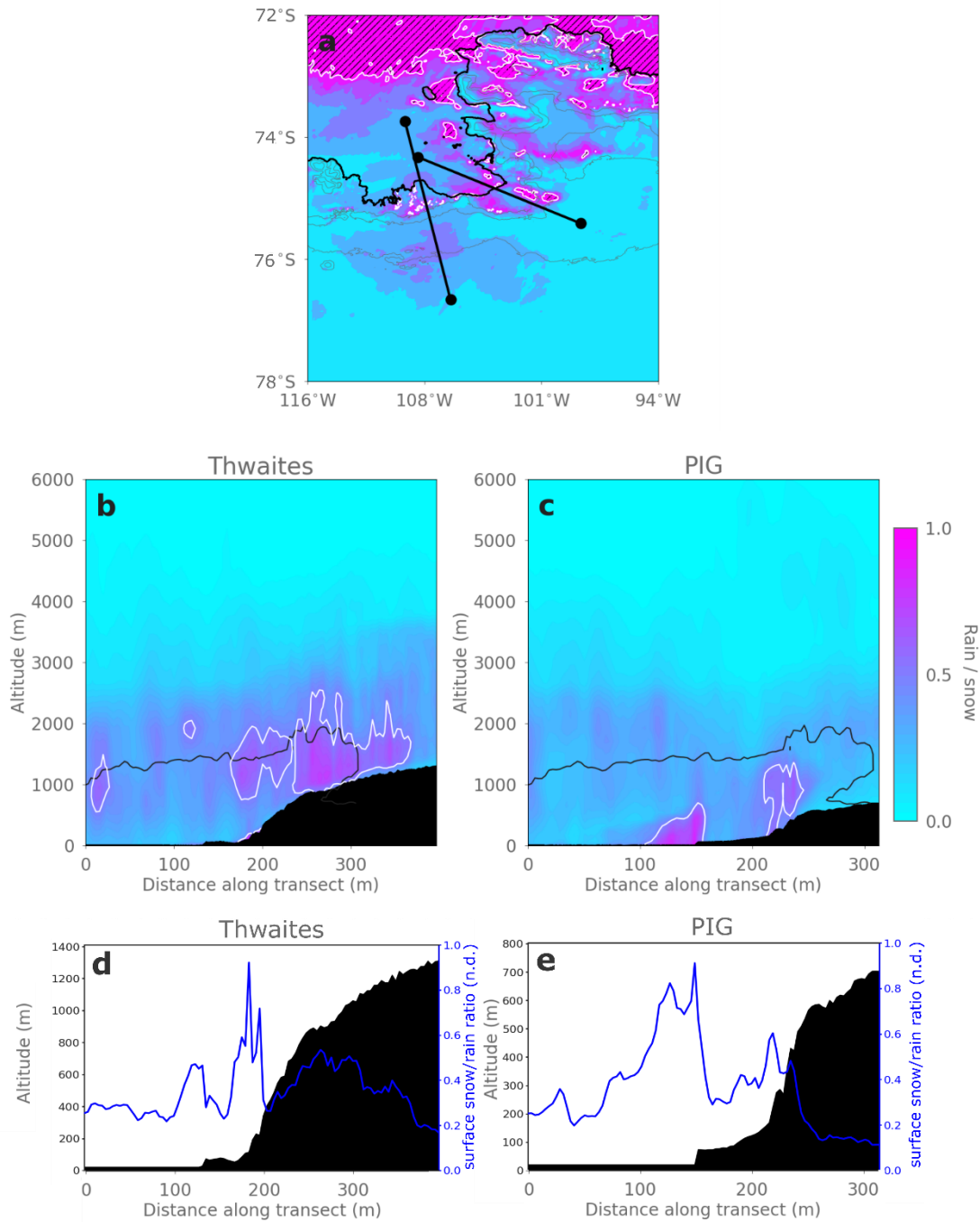
Figure 7. Ratio of accumulated rain to snow averaged over the duration of the summer case (3-9 February 2020), expressed as rain / snow. Panel a) shows the mean ratio of accumulated rain / snow at the first model level, while panels b and c show transects of accumulated rain / snow along the transects through Thwaites Glacier and Pine Island Glacier indicated in panel a. Regions on the map in panel a where the ratio is above 1:1 (indicating that total rainfall is equivalent to or higher than total snowfall) are hatched. The dashed contour on panels b and c shows the maximum height of the 0°C air temperature threshold as in Figure 7, while the white contour outlines the region where the ratio of rain to snow is 1:2 or higher. Note the difference in colour scales used between panel a and panels b and c. Panels d and e show the rain:snow ratio at the surface along the Thwaites glacier (panel d) and Pine Island Glacier (panel e) transects, with the height of elevation indicated in black.

While rainfall does not occur frequently over the ASE in the current climate and is exclusively associated with extreme events like the ARs described here, these conditions may occur more often in future. Antarctic total precipitation amounts will increase with warming (by 5.5% per degree Celsius on average) and the number of extreme precipitation events and ARs over the ASE will probably continue to rise with global temperatures (Nicola et al., 2023). There is also some evidence that climate change may cause ARs to shift poleward, along with the storm track (Ma et al., 2020; Chemke, 2022). Although ARs are unlikely themselves to destabilise ice shelves like the TG ice shelf, they affect accumulation and so could change the timing of future mass loss from West Antarctic glaciers (Maclennan et al., 2023). For example, Donat-Magnin et al. (2020) use RCMs to show that ablation will increase over ASE ice shelves such as the PIG and TG ice shelves, primarily driven by increased melt and runoff rates, but that the ratio of melting to snowfall is still low compared to other Antarctic ice shelves like the Ross or Filchner-Ronne. This is corroborated by Gilbert & Kittel (2021), which shows that even under a high-emissions scenario, the risk of surface-driven West Antarctic ice shelf collapse is low until the end of the century because the amount of runoff is greatly outweighed by increased snowfall.

However, climate change will also increase the proportion of precipitation falling as rain, as has been shown for the Arctic (McCrystall et al., 2021). For instance, Donat-Magnin et al. (2021) show that rain occurs on 0.5 and 1 day per year over the TG and PIG, respectively, in the current climate but that this may increase to 4.2 and 5.8 per year by 2100. These changes to total precipitation and the phase of precipitation are extremely important for determining ice sheet and ice shelf SMB. For example, rain-on-snow events can cause the surface to darken, reducing surface albedo and enhancing melt via the melt-albedo feedback (Box et al., 2022; Stroeve et al., 2022). As the climate warms, the future of Antarctic precipitation phase will remain an extremely pertinent subject of research.

3.5 Impact of resolution on precipitation

As noted in section 1, model resolution can strongly determine the amount of precipitation simulated, especially in regions with steep topography and where precipitation is dominated by orographic processes, such as those we have shown to be occurring here.

As shown in Figure 3 and Table 2, the RCMs simulate higher accumulated snow and rainfall totals than ERA5, which is likely related to resolution. At ~31 km, the resolution of ERA5 is considerably coarser than the resolution of the 1 km innermost RCM nests. One of the variables for which this is most apparent is air temperature. As shown in Table 2, all three RCMs indicate much warmer median air temperatures over the TG and PIG ice shelves than ERA5, suggesting the lower resolution of ERA5 is not sufficient to capture the topographic modification of the AR. The absolute maximum temperatures are also lower, with median air temperatures over the PIG and TG ice shelves approximately 10°C lower in ERA5 than the RCMs in both cases (Table 2). The agreement between the RCMs, all of which are forced by ERA5, suggests that the representation of complex topography is the cause of this difference, rather than internal model differences. This indicates that high resolution

is necessary to capture the complex interactions between large-scale, mesoscale and local meteorological processes which are important during such conditions in this region, and that RCMs are required to reproduce the factors governing the drivers and impacts of AR events in regions with complex topography.

630 However, there is a trade-off when conducting simulations between resolution and computational efficiency, so it is worth investigating what kind of resolution is sufficient to capture the dynamics of extreme precipitation in this region. To explore this, Figure 8 shows accumulated snow and rainfall totals during the summer case across the three different resolution nests of the MetUM: 1 km, 3 km and 12 km grid spacing.

635 There are few differences in accumulated snowfall amounts between the various resolution domains of the MetUM, indicating that simulated snowfall totals are comparatively insensitive to resolution. Given that snowfall dominates over rainfall, this suggests that the model can capture the dominant drivers of extreme precipitation, even at the relatively coarser resolution of 12 km. However, there is still some advantage to using higher resolution to capture finer-scale spatial variability when concentrating on smaller regions such as a single ice shelf. Furthermore, while total accumulated snowfall
640 in the 12 km simulation is comparable to 1 km totals, the accumulated rainfall totals over TG ice shelf are 16 times lower in the 12 km simulation compared to the 1 km simulations during the summer case and 4 times lower during the winter case (Figure 8). Across the entire domain, rain is simulated only over the steepest terrain, such as Thurston Island and King Peninsula. Because considerably less rain falls than snow, this has a fairly minimal effect on total accumulated precipitation. Nonetheless, this suggests that sub-grid scale processes may not be parameterised adequately at coarser resolutions, for
645 example the sub-grid phase partitioning of cloud, or the microphysical processes controlling the generation of supercooled drizzle. These are known problems with the MetUM (Gilbert et al., 2020; Bodas-Salcedo et al., 2016; Abel et al., 2017) and other RCMs (Hyder et al., 2018; Vergara-Temprado et al., 2018), especially in Antarctica and the Southern Ocean. This suggests that while coarser resolution configurations of RCMs can capture the large-scale characteristics of precipitation extremes, finer grid scales are required to fully capture the complex interactions producing liquid precipitation in this region.
650
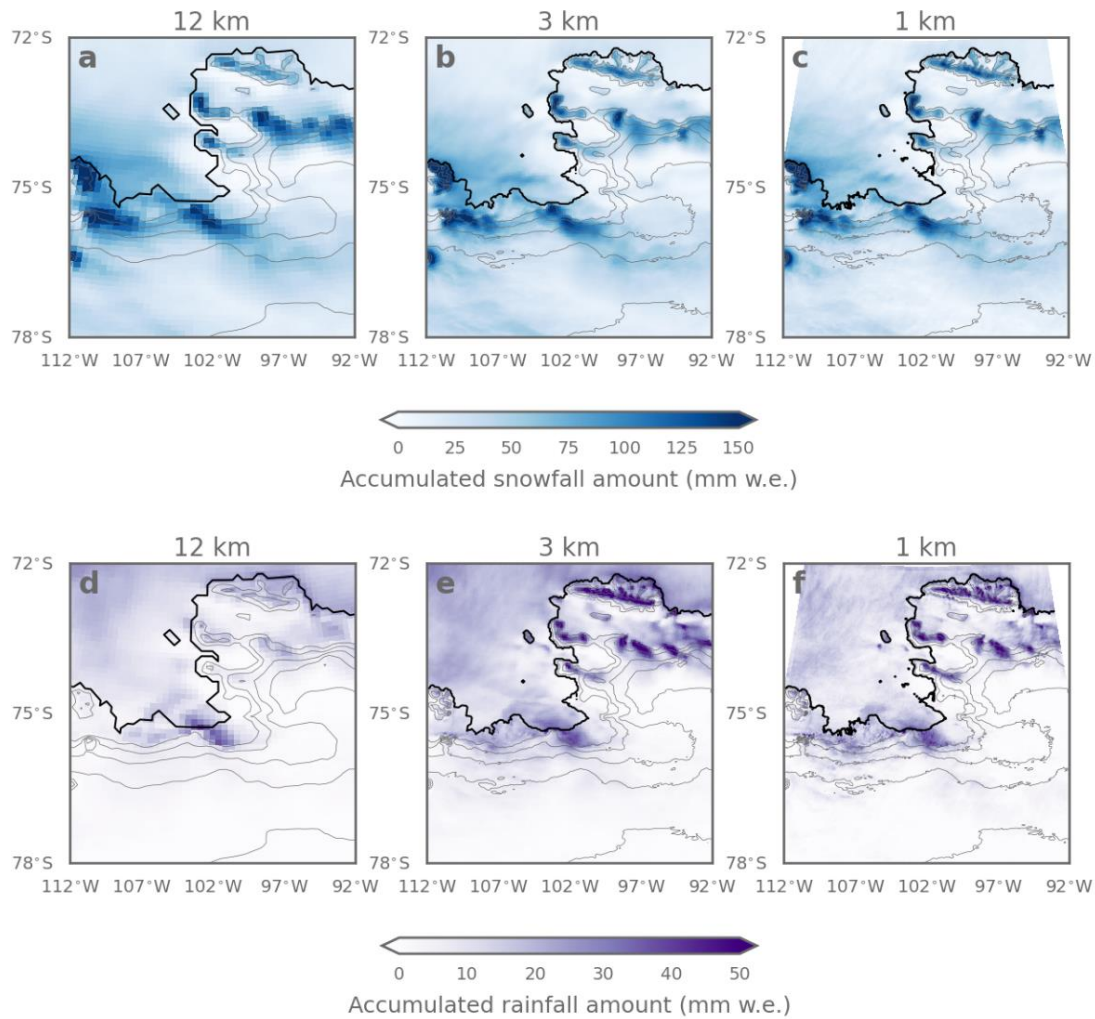
Figure 8. Accumulated snowfall (a-c) and rainfall (d-f) during the summer case (3-9 February 2020), as simulated by the MetUM at 12 km, 3 km and 1 km horizontal grid spacing.

655

4 Conclusions

660 We have used a mini-ensemble of state-of-the-art RCMs to explore the characteristics of extreme precipitation events in West Antarctica. Precipitation totals are especially high when the AR interacts with complex topography, generating snow and rain as a result of orographic uplift and allowing warm conditions favourable to liquid precipitation to persist via latent heating and foehn conditions near the surface.

665 We have shown that estimates of precipitation produced by the three RCMs are consistent with observations and with each other. For example, they simulate snowfall totals that are of comparable magnitude to *in situ* measurements of snow accumulation. However, all RCMs underestimate the amount of snowfall at both sites and do not capture the observed differences between stations, suggesting that there are highly localised, unresolved processes influencing snowfall.

670 The broad patterns of rain and snowfall are captured in ERA5 and all RCMs. Considering ice shelf-averaged totals as well as the spatial distribution of precipitation, Polar-WRF and the MetUM simulate extremely similar cumulative summer snow and rainfall amounts, with HCLIM and ERA5 producing relatively less over the ice shelves of interest. However, during winter, the MetUM simulates more rain over the TG and PIG ice shelves, and much higher rainfall totals over the steepest terrain in the domain. The simulated amount of rain falling in both cases is non-trivial, especially during the summer case
675 when up to 30 mm w.e. falls over some parts of the domain. However, two of the RCMs indicate that small amounts of rain may be falling even during the winter case, when temperatures are almost entirely below freezing. The lack of *in situ* rainfall observations means this is impossible to verify, but the occurrence of rain in all three RCMs, ERA5 and SNOWPACK in summer, and in two out of three of the RCMs in winter supports the idea that rain is indeed falling over this region.

680 The RCMs compare more favourably against observations than ERA5 reanalysis, which is unable to capture the dynamics of these events seen in the RCM output. ERA5 has been used extensively to assess the impacts of ARs in Antarctica, but we have shown that it has insufficient resolution to capture the interaction between ARs and steep topography. This is a limitation considering that the most extreme and high-impact events often result from the combination of ARs with topographically induced phenomena like foehn events and may suggest that impacts have been previously underestimated.
685 We further evaluated the differences between MetUM simulations at varying resolution. The MetUM exhibits a convergence across resolution with respect to total precipitation, indicating that the coarser resolution 12 km domain is sufficient to capture its large-scale dynamics and drivers. However, the 12 km MetUM configuration does not represent the phase of precipitation as accurately as higher resolutions, suggesting that km-scale resolution is required for an accurate assessment of precipitation phase. Furthermore, for very detailed studies of the microphysical processes contributing to
690 precipitation, finer resolutions – in this case 1 km – offer considerable benefits over configurations at ~10 km scale. This work therefore emphasises the importance of RCMs for examining the dynamics, origins and development of ARs in regions

with complex topography. Additional sensitivity experiments, for example exploring the impact of specific microphysical parameters and processes like droplet or ice crystal number, are beyond the scope of this study but would offer insight into the processes governing precipitation phase partitioning during extreme events.

695

Further analysis of the MetUM simulations shows that rain is formed via different processes. In summer in the presence of a near-surface warm pool, some rain forms when solid precipitation descends through the warm near-surface layer and melts. However, in colder conditions, such as over the TG transect in summer and over both locations in winter, super-cooled warm-rain processes act to form drizzle from liquid-bearing stratiform cloud in sub-zero temperatures. It is beyond

700 the scope of this study to explore either the cloud microphysical processes that produced rain in these cases or the specific impacts of rainfall on the stability of the TG and PIG ice shelves, but both would be fruitful avenues of further research. These findings emphasise the importance of using high-resolution modelling to fully capture the complex dynamics and processes occurring during these extreme events, as well as the need for further *in situ* precipitation measurements in this region, including of liquid precipitation. As climate change continues, rainfall is likely to become an increasingly regular

705 occurrence and further work must be done to understand its implications for melt-albedo feedback processes, latent heat release, and glacier and ice shelf surface mass balance in this critical region.

Data availability

ERA5 data are available via the Copernicus Climate Data Store (Hersbach et al., 2023). RCM data are archived at 10.5281/zenodo.12697647.AMIGOS AWS and snow sensor height data are available at https://www.usap-

710 dc.org/view/dataset/601549 while the SNOWPACK simulations are available at https://doi.org/10.5281/zenodo.7320237. The NASA GPM IMERG product used (in the supplement) is the IMERGHHR Final Precipitation L3 Half Hourly 0.1 Degree x 0.1 Degree V07 product (Huffman et al., 2023) and is available at https://doi.org/10.5067/GPM/IMERG/3B-HH/07.

Competing Interests

715 The authors declare no competing interests.

Acknowledgements

EG, JAT, DP, KV and AO acknowledge support from the PolarRES project, which has received funding from the European Union's Horizon 2020 research and innovation programme call H2020-LC-CLA-2018-2019-2020 under grant agreement number 101003590. EG also acknowledges the use of the ARCHER2 UK National Supercomputing Service

720 (https://www.archer2.ac.uk). MM acknowledges support from NASA FINESST grant 80NSSC21K1610. We are grateful to Jonathan Wille and one anonymous reviewer who provided helpful comments that strengthened the manuscript,

References

Abel, S.J., Boutle, I.A., Waite, K., Fox, S., Brown, P.R.A., Cotton, R., Lloyd, G., Choularton, T.W. and Bower, K.N. (2017) The role of precipitation in controlling the transition from stratocumulus to cumulus clouds in a Northern Hemisphere cold-air outbreak. Journal of the Atmospheric Sciences, 74(7), 2293–2314. https://doi.org/10.1175/JAS-D-16-0362.1.

Adusumilli, S., A Fish, M., Fricker, H. A., & Medley, B. (2021). Atmospheric river precipitation contributed to rapid increases in surface height of the west Antarctic ice sheet in 2019. *Geophysical Research Letters*, *48*(5), e2020GL091076. https://doi.org/10.1029/2020GL091076

Alley, K., Scambos, T., Siegfried, M. *et al.* (2016) Impacts of warm water on Antarctic ice shelf stability through basal channel formation. *Nature Geosci* **9**, 290–293. https://doi.org/10.1038/ngeo2675

Alley, K. E., Wild, C. T., Luckman, A., Scambos, T. A., Truffer, M., Pettit, E. C., ... & Dunmire, D. (2021). Two decades of dynamic change and progressive destabilization on the Thwaites Eastern Ice Shelf. *The Cryosphere*, *15*(11), 5187-5203. https://doi.org/10.5194/tc-15-5187-2021

Baiman, R., Winters, A. C., Pohl, B., Favier, V., Wille, J. D., & Clem, K. R. (2024). Synoptic and planetary-scale dynamics modulate Antarctic atmospheric river precipitation intensity. Communications Earth & Environment, 5(1), 127. https://doi.org/10.1038/s43247-024-01307-9

Balsamo, G., Beljaars, A., Scipal, K., Viterbo, P., v. d. Hurk, B., Hirschi, M., and Betts, A. K. (2009). A Revised Hydrology for the ECMWF Model: Verification from Field Site to Terrestrial Water Storage and Impact in the Integrated Forecast System, J. Hydrometeorol., 10, 623–643, https://doi.org/10.1175/2008JHM1068.1,

Bengtsson, L., Andrae, U., Aspelien, T., Batrak, Y., Calvo, J., de Rooy, W., Gleeson, E., Hansen-Sass, B., Homleid, M., Hortal, M., Ivarsson, K.-I., Lenderink, G., Niemelä, S., Nielsen, K. P., Onvlee, J., Rontu, L., Samuelsson, P., Muñoz, D. S., Subias, A., Tijm, S., Toll, V., Yang, X., and Køltzow, M. Ø. (2017) The HARMONIE–AROME Model Configuration in the ALADIN–HIRLAM NWP System, Mon. Weather Rev., 145, 1919–1935, https://doi.org/10.1175/MWR-D-16-0417.1.

Belušić D, de Vries H, Dobler A et al (2020) HCLIM38: a flexible regional climate model applicable for different climate zones from coarse to convection-permitting scales. Geosci Model Dev 13(3):1311–1333. https://doi.org/10.5194/gmd-13-1311-2020

755 Bodas-Salcedo, A., Hill, P. G., Furtado, K., Williams, K. D., Field, P. R., Manners, J. C., Hyder, P., & Kato, S. (2016a). Large contribution of supercooled liquid clouds to the solar radiation budget of the Southern Ocean. *Journal of Climate*, **29**(11), 4213–4228. https://doi.org/10.1175/JCLI-D-15-0564.1

Boutle, I. A., Eyre, J. E. J., ^ Lock, A. P. (2014) Seamless stratocumulus simulation across the turbulent gray zone, Mon.
760 Weather Rev., 142, 1655–1668, https://doi.org/10.1175/MWR-D-13-00229.1.

Box, J. E., Wehrlé, A., van As, D., Fausto, R. S., Kjeldsen, K. K., Dachauer, A., ... & Picard, G. (2022). Greenland ice sheet rainfall, heat and albedo feedback impacts from the mid-August 2021 atmospheric river. *Geophysical Research Letters*, *49*(11), e2021GL097356. https://doi.org/10.1029/2021GL097356

765
Box, J. E., Nielsen, K. P., Yang, X., Niwano, M., Wehrlé, A., van As, D., ... & Noël, B. (2023). Greenland ice sheet rainfall climatology, extremes and atmospheric river rapids. *Meteorological Applications*, *30*(4), e2134. https://doi.org/10.1002/met.2134

770 Bozkurt, D., Rondanelli, R., Marín, J. C., & Garreaud, R. (2018). Foehn event triggered by an atmospheric river underlies record-setting temperature along continental Antarctica. *Journal of Geophysical Research: Atmospheres*, 123(8), 3871-3892. https://doi.org/10.1002/2017JD027796

Bozkurt, D., Carrasco, J., Cordero, R., Fernandoy, F., Gómez, A., Carrillo, B., & Guan, B. (2024). Atmospheric river brings
775 warmth and rainfall to the northern Antarctic Peninsula during the mid-austral winter of 2023. *Geophysical Research Letters*, 51, e2024GL108391, https://doi.org/10.1029/2024GL108391.

Bromwich, D. H., F. O. Otieno, K. M. Hines, K. W. Manning, and E. Shilo (2013), Comprehensive evaluation of polar weather research and forecasting model performance in the Antarctic, . *Journal of Geophysical Research: Atmospheres*, 118, 274–292,
780 doi:10.1029/2012JD018139.

Bromwich, D. H., Gorodetskaya, I. V., Carpentier, S., Alexander, S., Bazile, E., Heinrich, V. J., ... & Zou, X. (2024) Winter Targeted Observing Periods during the Year of Polar Prediction in the Southern Hemisphere (YOPP-SH). Bull. Amer. Meteor. Soc., 105, E1662–E1684, https://doi.org/10.1175/BAMS-D-22-0249.1

785
Bush, M., Boutle, I., Edwards, J., Finnenkoetter, A., Franklin, C., Hanley, K., ... & Weeks, M. (2023). The second Met Office Unified Model–JULES Regional Atmosphere and Land configuration, RAL2. *Geoscientific Model Development*, *16*(6), 1713-1734. https://doi.org/10.5194/gmd-16-1713-2023

790 Carter, J., Leeson, A., Orr, A., Kittel, C., & van Wessem, J. M. (2022). Variability in Antarctic surface climatology across regional climate models and reanalysis datasets. *The Cryosphere*, *16*(9), 3815-3841. https://doi.org/10.5194/tc-16-3815-2022

Chemke, R. (2022). The future poleward shift of Southern Hemisphere summer mid-latitude storm tracks stems from ocean coupling. Nature Communications, 13(1), 1730. https://doi.org/10.1038/s41467-022-29392-4

795

Chen, F., and J. Dudhia, 2001: Coupling an Advanced Land Surface–Hydrology Model with the Penn State–NCAR MM5 Modeling System. Part I: Model Implementation and Sensitivity. Mon. Wea. Rev., 129, 569–585, https://doi.org/10.1175/1520-0493(2001)129<0569:CAALSH>2.0.CO;2.

800 Clapeyron, B. P. E. (1834). Memoir sur la puissance motrice de la chaleur. Journal de l'École royale polytechnique, 153-190. Clausius, R. (1850). Ueber die bewegende Kraft der Wärme und die Gesetze, welche sich daraus für die Wärmelehre selbst ableiten lassen. Annalen der Physik, 155(3), 368-397. https://doi.org/10.1002%2Fandp.18501550403

Cullen, M. J. P. (1993) The unified forecast/climate model. Meteorol. Mag., 122:81–94.

805

de Rooy, W. C. & Siebesma, A. P. (2008) A Simple Parameterization for Detrainment in Shallow Cumulus, Mon. Weather Rev., 136, 560–576, https://doi.org/10.1175/2007MWR2201.1

Donat-Magnin, M., Jourdain, N. C., Kittel, C., Agosta, C., Amory, C., Gallée, H., ... & Chekki, M. (2021). Future surface mass
810 balance and surface melt in the Amundsen sector of the West Antarctic Ice Sheet. *The Cryosphere*, *15*(2), 571-593. https://doi.org/10.5194/tc-15-571-2021

Doyle, S. H., Hubbard, A., Van De Wal, R. S., Box, J. E., Van As, D., Scharrer, K., ... & Hubbard, B. (2015). Amplified melt and flow of the Greenland ice sheet driven by late-summer cyclonic rainfall. Nature Geoscience, 8(8), 647-653. Nature
815 Geosci 8, 647–653 https://doi.org/10.1038/ngeo2482

Eckert, E., Hudak, D., Mekis, É., Rodriguez, P., Zhao, B., Mariani, Z., ... & Walker, K. A. (2022). Validation of the Final Monthly Integrated Multisatellite Retrievals for GPM (IMERG) Version 05 and Version 06 with Ground-Based Precipitation Gauge Measurements across the Canadian Arctic. *Journal of Hydrometeorology*, *23*(5), 715-731.
820 https://doi.org/10.1175/JHM-D-21-0040.1

ECMWF: Part IV: Physical Processes, in: IFS Documentation CY41R2, IFS Documentation, ECMWF, https://doi.org/10.21957/tr5rv27xu, 2016.

825 Elvidge, A. D., & Renfrew, I. A. (2016). The causes of foehn warming in the lee of mountains. *Bulletin of the American Meteorological Society*, **97**(3), 455–466. https://doi.org/10.1175/BAMS-D-14-00194.1

Fernández-González, S., F. Valero, J. L. Sánchez, E. Gascón, L. López, E. García-Ortega, and A. Merino (2015), Analysis of a seeder-feeder and freezing drizzle event, J. Geophys. Res. Atmos., 120, 3984–3999, doi:10.1002/2014JD022916.

830 Field, P. R., Heymsfield, A. J., & Bansemer, A. (2007) Snow Size Distribution Parameterization for Midlatitude and Tropical Ice Clouds, J. Atmos. Sci., 64, 4346–4365, https://doi.org/10.1175/2007JAS2344.1.

Finlon, J. A., Rauber, R. M., Wu, W., Zaremba, T. J., McFarquhar, G. M., Nesbitt, S. W., ... & DeMott, P. J. (2020). Structure
835 of an atmospheric river over Australia and the Southern Ocean: II. Microphysical evolution. Journal of Geophysical Research: Atmospheres, 125(18), e2020JD032514. https://doi.org/10.1029/2020JD032513

Gehring, J., Vignon, É., Billault-Roux, A. C., Ferrone, A., Protat, A., Alexander, S. P., & Berne, A. (2022). Orographic flow influence on precipitation during an atmospheric river event at Davis, Antarctica. *Journal of Geophysical Research:*
840 *Atmospheres*, *127*(2), e2021JD035210. https://doi.org/10.1029/2021JD035210

Gilbert, E., Orr, A., King, J. C., Renfrew, I. A., Lachlan-Cope, T., Field, P. F., & Boutle, I. A. (2020). Summertime cloud phase strongly influences surface melting on the Larsen C ice shelf, Antarctica. *Quarterly Journal of the Royal Meteorological Society*, *146*(729), 1575-1589. https://doi.org/10.1002/qj.3753

845 Gilbert, E., & Kittel, C. (2021). Surface melt and runoff on Antarctic ice shelves at 1.5 C, 2 C, and 4 C of future warming. *Geophysical Research Letters*, *48*(8), e2020GL091733. https://doi.org/10.1029/2020GL091733

Gilbert, E., Orr, A., King, J. C., Renfrew, I. A., & Lachlan-Cope, T. (2022). A 20-Year Study of Melt Processes Over Larsen
850 C Ice Shelf Using a High-Resolution Regional Atmospheric Model: 1. Model Configuration and Validation. *Journal of Geophysical Research: Atmospheres*, *127*(8), e2021JD034766. https://doi.org/10.1029/2021JD034766

Gorodetskaya, I.V., Durán-Alarcón, C., González-Herrero, S. *et al.* Record-high Antarctic Peninsula temperatures and surface melt in February 2022: a compound event with an intense atmospheric river. *npj Clim Atmos Sci* **6**, 202 (2023).
855 https://doi.org/10.1038/s41612-023-00529-6

Harper, J., Saito, J., & Humphrey, N. (2023). Cold season rain event has impact on Greenland's firn layer comparable to entire summer melt season. Geophysical Research Letters, 50(14), e2023GL103654. https://doi.org/10.1029/2023GL103654

He, Y., Yi, F., Liu, F., Yin, Z., Yi, Y., Zhou, J., Yu, C. & Zhang, Y. (2022). Natural seeder-feeder process originating from mixed-phase clouds observed with polarization lidar and radiosonde at a mid-latitude plain site. *Journal of Geophysical Research: Atmospheres,* 127(5), e2021JD036094. https://doi.org/10.1029/2021JD036094

Hersbach, H., Bell, B., Berrisford, P., Hirahara, S., Horányi, A., Muñoz-Sabater, J., ... & Thépaut, J. N. (2020). The ERA5 global reanalysis. *Quarterly Journal of the Royal Meteorological Society*, *146*(730), 1999-2049. https://doi.org/10.1002/qj.3803

Hersbach, H., Bell, B., Berrisford, P., Biavati, G., Horányi, A., Muñoz Sabater, J., Nicolas, J., Peubey, C., Radu, R., Rozum, I., Schepers, D., Simmons, A., Soci, C., Dee, D., Thépaut, J-N. (2023a): ERA5 hourly data on single levels from 1940 to present. Copernicus Climate Change Service (C3S) Climate Data Store (CDS), DOI: 10.24381/cds.adbb2d47 (Accessed on 05-05-2023)

Hines, K. M., Bromwich, D. H., Wang, S.-H., Silber, I., Verlinde, J., and Lubin, D. (2019) Microphysics of summer clouds in central West Antarctica simulated by the Polar Weather Research and Forecasting Model (WRF) and the Antarctic Mesoscale Prediction System (AMPS), Atmos. Chem. Phys., 19, 12431–12454, https://doi.org/10.5194/acp-19-12431-2019 .

Huffman, G.J., E.F. Stocker, D.T. Bolvin, E.J. Nelkin, Jackson Tan (2023), GPM IMERG Final Precipitation L3 Half Hourly 0.1 degree x 0.1 degree V07, Greenbelt, MD, Goddard Earth Sciences Data and Information Services Center (GES DISC), Accessed: *04 November 2023*, 10.5067/GPM/IMERG/3B-HH/07

Hyder, P., Edwards, J., Allan, R.P. *et al.* (2018) Critical Southern Ocean climate model biases traced to atmospheric model cloud errors. *Nat Commun* **9**, 3625 (2018). https://doi.org/10.1038/s41467-018-05634-2

Iacono, M. J., J. S. Delamere, E. J. Mlawer, M. W. Shephard, S. A. Clough, and W. D. Collins (2008), Radiative forcing by long-lived greenhouse gases: Calculations with the AER radiative transfer models, J. Geophys. Res., 113, D13103, doi:10.1029/2008JD009944.

Iles, C. E., Vautard, R., Strachan, J., Joussaume, S., Eggen, B. R., and Hewitt, C. D. (2020) The benefits of increasing resolution in global and regional climate simulations for European climate extremes, Geosci. Model Dev., 13, 5583–5607, https://doi.org/10.5194/gmd-13-5583-2020.

890

IPCC, 2019: IPCC Special Report on the Ocean and Cryosphere in a Changing Climate [H.-O. Pörtner, D.C. Roberts, V. Masson-Delmotte, P. Zhai, M. Tignor, E. Poloczanska, K. Mintenbeck, A. Alegría, M. Nicolai, A. Okem, J. Petzold, B. Rama, N.M. Weyer (eds.)]. Cambridge University Press, Cambridge, UK and New York, NY, USA, 755 pp. https://doi.org/10.1017/9781009157964.

895

Kain, J. S., 2004: The Kain–Fritsch Convective Parameterization: An Update. J. Appl. Meteor. Climatol., 43, 170–181, https://doi.org/10.1175/1520-0450(2004)043<0170:TKCPAU>2.0.CO;2.

Keenan, E., Wever, N., Dattler, M., Lenaerts, J. T., Medley, B., Kuipers Munneke, P., & Reijmer, C. (2021). Physics-based
900 SNOWPACK model improves representation of near-surface Antarctic snow and firn density. *The Cryosphere*, *15*(2), 1065-1085. https://doi.org/10.5194/tc-15-1065-2021

Laprise, R. (1992) The Euler equations of motion with hydrostatic pressure as an independent variable. Mon. Wea. Rev., 120, 197–207, doi:10.1175/1520-0493

905

Lascaux, F., Richard, E., & Pinty, J.-P. (2006) Numerical simulations of three different MAP IOPs and the associated microphysical processes, Q. J. Roy. Meteorol. Soc., 132, 1907–1926, https://doi.org/10.1256/qj.05.197

Lean HW, Clark PA. 2003. High resolution modelling of orographic rainfall. *American Meteorological Society 10th*
910 *Conference on Mesoscale Processes*, Paper 6.7.

Lehning, M., Bartelt, P., Brown, B., Russi, T., Stöckli, U., & Zimmerli, M. (1999) snowpack model calculations for avalanche warning based upon a new network of weather and snow stations, Cold Reg. Sci. Technol., 30, 145–157, https://doi.org/10.1016/S0165- 232X(99)00022-1.

915

Lehning, M., Bartelt, P., Brown, B., & Fierz, C. (2002a) A physical SNOWPACK model for the Swiss avalanche warning: Part III: meteorological forcing, thin layer formation and evaluation, Cold Reg. Sci. Technol., 35, 169–184, https://doi.org/10.1016/S0165- 232X(02)00072-1 .

920 Lehning, M., Bartelt, P., Brown, B., Fierz, C., & Satyawali, P. (2002b) A physical SNOWPACK model for the Swiss avalanche warning: Part II. Snow microstructure, Cold Reg. Sci. Technol., 35, 147– 167, https://doi.org/10.1016/S0165-232X(02)00073-3

Lenaerts, J. T. M., Medley, B., van den Broeke, M. R. & Wouters, B. (2019) Observing and Modeling Ice Sheet Surface Mass Balance. Reviews of Geophysics 57 (2) 376-420. https://doi.org/10.1029/2018RG000622

Lhermitte, S., Sun, S., Shuman, C., Wouters, B., Pattyn, F., Wuite, J., Berthier, E. and Nagler, T., 2020. Damage accelerates ice shelf instability and mass loss in Amundsen Sea Embayment. *Proceedings of the National Academy of Sciences*, *117*(40), pp.24735-24741. https://www.pnas.org/doi/epdf/10.1073/pnas.1912890117

Lindstedt, D., Lind, P., Kjellström, E., and Jones, C. (2015) A new regional climate model operating at the meso-gamma scale: performance over Europe, Tellus A: Dynam. Meteorol. Oceanogr., 67, 24138, https://doi.org/10.3402/tellusa.v67.24138.

Lock, A. P., Brown, A. R., Bush, M. R., Martin, G. M., & Smith, R. N. B. (2000) A new boundary layer mixing scheme. Part I: Scheme description and single-column model tests, Mon. Weather Rev., 128, 3187–3199, https://doi.org/10.1175/15200493(2000)1282.0.CO;2

Lu, H., Orr, A., King, J., Phillips, T., Gilbert, E., Colwell, S., & Bracegirdle, T. J. (2023). Extreme warm events in the South Orkney Islands, Southern Ocean: Compounding influence of atmospheric rivers and föhn conditions. Quarterly Journal of the Royal Meteorological Society, 149(757), 3645-3668. https://doi.org/10.1002/qj.4578

Ma, W., Chen, G., & Guan, B. (2020). Poleward shift of atmospheric rivers in the Southern Hemisphere in recent decades. *Geophysical Research Letters*, *47*(21), e2020GL089934. https://doi.org/10.1029/2020GL089934

Maclennan, M. L., Lenaerts, J., Shields, C. A., Hoffman, A. O., Wever, N., Thompson-Munson, M., ... & Wille, J. D. (2023). Climatology and surface impacts of atmospheric rivers on West Antarctica. *The Cryosphere*, *17*(2), 865-881. https://doi.org/10.5194/tc-17-865-2023

Marshall, H. P., Conway, H., & Rasmussen, L. A. (1999). Snow densification during rain. Cold Regions Science and Technology, 30(1-3), 35-41. https://doi.org/10.1016/S0165-232X(99)00011-7

Medley, B., Thomas, E.R. (2019) Increased snowfall over the Antarctic Ice Sheet mitigated twentieth-century sea-level rise. *Nature Clim Change* **9**, 34–39. https://doi.org/10.1038/s41558-018-0356-x

Morcrette, J.-J., Barker, H., Cole, J., Iacono, M. and Pincus, R. (2008). Impact of a new radiation package, McRad, in the ECMWF Integrated Forecasting System. Mon. Wea. Rev., 136, 4773–4798. https://doi.org/10.1175/2008MWR2363.1

Morlighem, M. (2022). MEaSUREs BedMachine Antarctica, Version 3 [Data Set]. Boulder, Colorado USA. NASA National Snow and Ice Data Center Distributed Active Archive Center. https://doi.org/10.5067/FPSU0V1MWUB6. Date Accessed 04-11-2024.

960 Morrison, H., Thompson, G. & Tatarskii, V. (2008) Impact of cloud microphysics on the development of trailing stratiform precipitation in a simulated squall line: Comparison of one- and two-moment schemes. Mon. Wea. Rev. , 137, 991-1007. https://ui.adsabs.harvard.edu/link_gateway/2009MWRv..137..991M/doi:10.1175/2008MWR2556.1

Morrison, H., van Lier-Walqui, M., Fridlind, A. M., Grabowski, W. W., Harrington, J. Y., Hoose, C., ... & Xue, L. (2020).
965 Confronting the challenge of modeling cloud and precipitation microphysics. Journal of advances in modeling earth systems, 12 (8), e2019MS001689. https://doi.org/10.1029/2019MS001689

Mottram, R., Hansen, N., Kittel, C., van Wessem, J. M., Agosta, C., Amory, C., Boberg, F., van de Berg, W. J., Fettweis, X., Gossart, A., van Lipzig, N. P. M., van Meijgaard, E., Orr, A., Phillips, T., Webster, S., Simonsen, S. B. & Souverijns, N.
970 (2020) What is the surface mass balance of Antarctica? An intercomparison of regional climate model estimates. The Cryosphere 15 (8) 3751-3784. https://doi.org/10.5194/tc-15-3751-2021.

Müller, M., Homleid, M., Ivarsson, K.-I., Køltzow, M. A. Ø., Lindskog, M., Midtbø, K. H., Andrae, U., Aspelien, T., Berggren, L., Bjørge, D., Dahlgren, P., Kristiansen, J., Randriamampianina, R., Ridal, M., & Vignes, O. (2017) AROME-MetCoOp: A
975 Nordic Convective-Scale Operational Weather Prediction Model, Weather Forecast., 32, 609–627, https://doi.org/10.1175/WAFD-16-0099.1

Nakanishi, M., Niino, H. An Improved Mellor–Yamada Level-3 Model: Its Numerical Stability and Application to a Regional Prediction of Advection Fog. Boundary-Layer Meteorol 119, 397–407 (2006). https://doi.org/10.1007/s10546-005-9030-8
980

Nicola, L., Notz, D., & Winkelmann, R. (2023) Revisiting temperature sensitivity: how does Antarctic precipitation change with temperature?, The Cryosphere, 17, 2563–2583, https://doi.org/10.5194/tc-17-2563-2023

Ning, W., Wang, Y., Zhang, W., & Zhou, M. (2024). What recent global atmospheric reanalyses and regional climate models
985 can represent observed snow accumulation on Antarctica?. Atmospheric Research, 300, 107260. https://doi.org/10.1016/j.atmosres.2024.107260

Noël, B., Lenaerts, J.T.M., Lipscomb, W.H. et al. Peak refreezing in the Greenland firn layer under future warming scenarios. Nat Commun 13, 6870 (2022). https://doi.org/10.1038/s41467-022-34524-x

990

Pinty, J. P., & Jabouille, P. (1998). A mixed-phase cloud parameterization for use in mesoscale non-hydrostatic model: simulations of a squall line and of orographic precipitations. In Conf. on cloud physics (pp. 217-220). Everett, WA: Amer. Meteor. Soc..

995 Pradhan, R. K., Markonis, Y., Godoy, M. R. V., Villalba-Pradas, A., Andreadis, K. M., Nikolopoulos, E. I., ... & Hanel, M. (2022). Review of GPM IMERG performance: A global perspective. Remote Sensing of Environment, 268, 112754. https://doi.org/10.1016/j.rse.2021.112754

Pritchard, H. D. (2021). Global data gaps in our knowledge of the terrestrial cryosphere. Frontiers in Climate, 3, 689823.
1000 https://doi.org/10.3389/fclim.2021.689823

Ramelli, F., Henneberger, J., David, R. O., Bühl, J., Radenz, M., Seifert, P., ... & Lohmann, U. (2021). Microphysical investigation of the seeder and feeder region of an Alpine mixed-phase cloud. *Atmospheric Chemistry and Physics*, *21*(9), 6681-6706. https://doi.org/10.5194/acp-21-6681-2021
1005

Rignot, E., Mouginot, J., Scheuchl, B., van den Broeke, M. R., van Wessem, M. J. & Morlighem, M. (2019) Four decades of Antarctic Ice Sheet mass balance from 1979–2017. Proceedings of the National academy of Sciences 116 (4) https://doi.org/10.1073/pnas.1812883116

1010 Scambos, T., Ross, R., Haran, T., Bauer, R., Ainley, D., Seo, K., . . . MacAyeal, D. (2013). A camera and multisensor automated station design for polar physical and biological systems monitoring: AMIGOS. *Journal of Glaciology, 59*(214), 303-314. doi:10.3189/2013JoG12J170

Scambos, T. A., Bell, R. E., Alley, R. B., Anandakrishnan, S., Bromwich, D. H., Brunt, K., ... & Yager, P. L. (2017). How
1015 much, how fast?: A science review and outlook for research on the instability of Antarctica's Thwaites Glacier in the 21st century. *Global and Planetary Change*, *153*, 16-34. https://doi.org/10.1016/j.gloplacha.2017.04.008

Schmucki, E., Marty, C., Fierz, C., & Lehning, M. (2014) Evaluation of modelled snow depth and snow water equivalent at three contrasting sites in Switzerland using SNOWPACK simulations driven by different meteorological data input, Cold Reg.
1020 Sci. Technol., 99, 27–37, https://doi.org/10.1016/J.COLDREGIONS.2013.12.004

Scott, R. C., Nicolas, J. P., Bromwich, D. H., Norris, J. R., & Lubin, D. (2019). Meteorological drivers and large-scale climate forcing of West Antarctic surface melt. Journal of Climate, 32(3), 665-684. https://doi.org/10.1175/JCLI-D-18-0233.1

1025   Shields, C. A., Wille, J. D., Marquardt Collow, A. B., Maclennan, M., & Gorodetskaya, I. V. (2022). Evaluating uncertainty and modes of variability for Antarctic atmospheric rivers. *Geophysical Research Letters*, *49*(16), e2022GL099577. https://doi.org/10.1029/2022GL099577

Simmons, A., and D. M. Burridge (1981) An energy and angular-momentum conserving vertical finite-difference scheme and
1030   hybrid vertical coordinates. Mon. Wea. Rev., 109, 758–766, doi:10.1175/1520-0493

Skamarock, W. C., Klemp, J. B., Dudhia, J., Gill, D. O., Liu, Z., Berner, J., … Huang, X. -yu. (2019). A Description of the Advanced Research Polar-WRF Model Version 4.1 (No. NCAR/TN-556+STR). https://doi.org/10.5065/1dfh-6p97

1035   Smith, B., Fricker, H. A., Gardner, A. S., Medley, B., Nilsson, J., Paolo, F. S., ... & Zwally, H. J. (2020). Pervasive ice sheet mass loss reflects competing ocean and atmosphere processes. Science, 368(6496), 1239-1242. https://doi.org/10.1126/science.aaz5845

Stroeve, J., Nandan, V., Willatt, R., Dadic, R., Rostosky, P., Gallagher, M., ... & Schneebeli, M. (2022). Rain on snow (ROS)
1040   understudied in sea ice remote sensing: a multi-sensor analysis of ROS during MOSAiC (Multidisciplinary drifting Observatory for the Study of Arctic Climate). *The Cryosphere*, *16*(10), 4223-4250. https://doi.org/10.5194/tc-16-4223-2022

Termonia, P., Fischer, C., Bazile, E., Bouyssel, F., Brožková, R., Bénard, P., Bochenek, B., Degrauwe, D., Derková, M., El Khatib, R., Hamdi, R., Mašek, J., Pottier, P., Pristov, N., Seity, Y., Smolíková, P., Španiel, O., Tudor, M., Wang, Y., Wittmann,
1045   C., and Joly, A.(2018) The ALADIN System and its canonical model configurations AROME CY41T1 and ALARO CY40T1, Geosci. Model Dev., 11, 257–281, https://doi.org/10.5194/gmd-11-257-2018.

van Wessem, J. M., van den Broeke, M. R., Wouters, B., & Lhermitte, S. (2023). Variable temperature thresholds of melt pond formation on Antarctic ice shelves. Nature Climate Change, 13(2), 161-166. https://doi.org/10.1038/s41558-022-01577-1
1050

Vergara-Temprado, J., Miltenberger, A. K., Furtado, K., Grosvenor, D. P., Shipway, B. J., Hill, A. A., ... & Carslaw, K. S. (2018). Strong control of Southern Ocean cloud reflectivity by ice-nucleating particles. *Proceedings of the National Academy of Sciences*, *115*(11), 2687-2692. https://doi.org/10.1073/pnas.1721627115

1055   Vignon, É., Roussel, M. L., Gorodetskaya, I. V., Genthon, C., & Berne, A. (2021). Present and future of rainfall in Antarctica. *Geophysical Research Letters*, *48*(8), e2020GL092281. https://doi.org/10.1029/2020GL092281

Walters, D., Baran, A. J., Boutle, I., Brooks, M., Earnshaw, P., Edwards, J., ... & Zerroukat, M. (2019). The Met Office Unified Model global atmosphere 7.0/7.1 and JULES global land 7.0 configurations. *Geoscientific Model Development*, *12*(5), 1909-1963. https://doi.org/10.5194/gmd-12-1909-2019

Wever, N., Schmid, L., Heilig, A., Eisen, O., Fierz, C., & Lehning, M. (2015) Verification of the multi-layer SNOWPACK model with different water transport schemes, The Cryosphere, 9, 2271–2293, https://doi.org/10.5194/tc-9-2271-2015 .

Wever, N. (2022). SNOWPACK simulations for Thwaites Cavity and Channel AMIGOS sites in West Antarctica [Data set]. Zenodo. https://doi.org/10.5281/zenodo.7320237

Wever, N., Keenan, E., Amory, C., Lehning, M., Sigmund, A., Huwald, H., & Lenaerts, J. (2023). Observations and simulations of new snow density in the drifting snow-dominated environment of Antarctica. *Journal of Glaciology, 69*(276), 823-840. doi:10.1017/jog.2022.102

Wille, J.D., Favier, V., Dufour, A. *et al.* (2019). West Antarctic surface melt triggered by atmospheric rivers. *Nat. Geosci.* **12**, 911–916 https://doi.org/10.1038/s41561-019-0460-1

Wille, J. D., Favier, V., Gorodetskaya, I. V., Agosta, C., Kittel, C., Beeman, J. C., ... & Codron, F. (2021). Antarctic atmospheric river climatology and precipitation impacts. *Journal of Geophysical Research: Atmospheres*, *126*(8), e2020JD033788. https://doi.org/10.1029/2020JD033788

Wille, J.D., Favier, V., Jourdain, N.C., Kittel, C., Turton, J.V., Agosta, C., Gorodetskaya, I.V., Picard, G., Codron, F., Santos, C.L.D. and Amory, C., 2022. Intense atmospheric rivers can weaken ice shelf stability at the Antarctic Peninsula. *Communications Earth & Environment*, *3*(1), p.90. https://doi.org/10.1038/s43247-022-00422-9

Wille, J. D., Alexander, S. P., Amory, C., Baiman, R., Barthélemy, L., Bergstrom, D. M., ... & Zou, X. (2024). The extraordinary March 2022 East Antarctica "heat" wave. Part II: impacts on the Antarctic ice sheet. *Journal of Climate*, *37*(3), 779-799. https://doi.org/10.1175/JCLI-D-23-0176.1

Wilson, D. R. & Ballard, S. P. (1999) A microphysically based precipitation scheme for the UK Meteorological Office Unified Model, Q. J. Roy. Meteor. Soc., 125, 1607–1636, https://doi.org/10.1002/qj.49712555707 .

Wilson, A. B., Bromwich, D. H. & Hines, K. M. (2011), Evaluation of Polar WRF forecasts on the Arctic System Reanalysis domain: Surface and upper air analysis, J. Geophys. Res., 116, D11112, doi:10.1029/2010JD015013

Wood, N., Staniforth, A., White, A., Allen, T., Diamantakis, M., Gross, M., Melvin, T., Smith, C., Vosper, S., Zerroukat, M., & Thuburn, J. (2014) An inherently mass-conserving semi-implicit semi-Lagrangian discretization of the deep-atmosphere global non-hydrostatic equations, Q. J. Roy. Meteorol. Soc., 140, 1505–1520, https://doi.org/10.1002/qj.2235.

Xu, K. M., & Randall, D. A. (1996) A semiempirical cloudiness parameterization for use in climate models. *J. Atmos. Sci.*, 53 (21) 3084–3102, https://doi.org/10.1175/1520-0469(1996)053<3084:ASCPFU>2.0.CO;2.

Xue, J., Xiao, Z., Bromwich, D. H. & Bai, L. (2022) Polar Polar-WRF V4.1.1 simulation and evaluation for the Antarctic and Southern Ocean. *Front. Earth Sci.*, **16**, 1005-1024, https://doi.org/10.1007/s11707-022-0971-8

Zou, X., Rowe, P. M., Gorodetskaya, I., Bromwich, D. H., Lazzara, M. A., Cordero, R. R., et al. (2023). Strong warming over the Antarctic Peninsula during combined atmospheric River and foehn events: Contribution of shortwave radiation and turbulence. *Journal of Geophysical Research: Atmospheres*, 128, e2022JD038138. https://doi.org/10.1029/2022JD038138